



## Migrating diurnal tide anomalies during QBO disruptions in 2016 and 2020: morphology and mechanism

Shuai Liu<sup>1,2</sup>, Guoying Jiang<sup>1,3,4</sup>, Bingxian Luo<sup>1,2</sup>, Xiao Liu<sup>5</sup>, Jiyao Xu<sup>1,3</sup>, Yajun Zhu<sup>1,3,4</sup>, and Wen Yi<sup>6,7</sup>

<sup>1</sup>State Key Laboratory of Solar Activity and Space Weather, National Space Science Center, Chinese Academy of Sciences, Beijing, 100190, China

<sup>2</sup>College of Earth and Planetary Sciences, University of Chinese Academy of Sciences, Beijing, 101408, China

<sup>3</sup>School of Astronomy and Space Science, University of Chinese Academy of Sciences, Beijing, 101408, China

<sup>4</sup>Hainan National Field Science Observation and Research Observatory for Space Weather, Danzhou, Hainan Province, China

<sup>5</sup>School of Mathematics and Statistics, Henan Normal University, Xinxiang, 453007, China

<sup>6</sup>CAS Key Laboratory of Geospace Environment, Department of Geophysics and Planetary Sciences, University of Science and Technology of China, Hefei, China

<sup>7</sup>CAS Center for Excellence in Comparative Planetology, Anhui Mengcheng Geophysics National Observation and Research Station, University of Science and Technology of China, Hefei, China

**Correspondence:** Guoying Jiang (gyjiang@swl.ac.cn) and Bingxian Luo (luobx@nssc.ac.cn)

Received: 3 June 2025 – Discussion started: 23 June 2025

Revised: 6 November 2025 – Accepted: 16 November 2025 – Published: 5 December 2025

**Abstract.** The stratosphere Quasi-Biennial Oscillation (QBO) modulates the migrating diurnal tide (DW1) in the mesosphere and lower thermosphere (MLT). DW1 amplitudes are larger during QBO westerly (QBOW) than during easterly (QBOE) phases. Since QBO's discovery in 1953, two rare QBO disruption events occurred in 2016 and 2020. During these events, anomalous westerly winds propagate upward, disrupting normal downward propagation of easterly phase and producing a persistent westerly wind layer. In this study, global responses of DW1 amplitudes and phases in MLT to these QBO disruptions, as well as their underlying mechanisms are investigated, using SABER/TIMED observations, MERRA-2 reanalysis and SD-WACCM-X simulations. Similarity of the DW1 responses to these two events is that DW1 phases and wavelengths exhibit close results to QBOW, whereas amplitudes lie between QBOW and QBOE. DW1 amplitudes in equatorial MLT (maximum difference) vary by 20.5 % and −10.2 % relative to QBOE and QBOW in 2016 event, but by 6.0 % and −21.1 % in 2020 event. In 2016 event, water-vapor radiative and latent heating, jointly modulated by the event and ENSO, increase significantly relative to QBOE. Less dissipation and less tidal energy removal in stratosphere along with gravity-wave (GW) drag in mesosphere tend to enhance DW1 amplitudes. In contrast, in 2020 event, water-vapor heating exhibits a 5 % increase. The dissipation and tidal energy removal has adverse effect on DW1, while GW drag exerts a weaker influence. The enhancement of water vapor heating together with the weaker GW drag likely accounts for the weaker enhancement of DW1 during this event.

## 1 Introduction

Atmospheric solar tides are planetary-scale harmonic waves with periods of a solar day. In the mesosphere and lower thermosphere (MLT), solar tides exert significant influences on atmospheric parameters such as wind, temperature, and density (Chapman and Lindzen, 1970; Xu et al., 2009; Jiang et al., 2010; Smith, 2012). Among these tides, the migrating diurnal tide (DW1) is one of the most prominent components. DW1 in MLT is modulated by external forcings, including the stratosphere Quasi-Biennial Oscillation (QBO; Hagan et al., 1999; Wu et al., 2008; Xu et al., 2009; Oberheide et al., 2009; Mukhtarov et al., 2009; Davis et al., 2013; Gan et al., 2014), El Niño–Southern Oscillation (ENSO; Lieberman et al., 2007; Cen et al., 2022) and 11-year solar cycle response (Singh and Gurubaran, 2017; Sun et al., 2022; Liu et al., 2024a, b). In this work, the impact of QBO is focused on.

The QBO dominates the variability of the equatorial stratosphere ( $\sim 16$ – $50$  km), shown as alternating downward propagating easterly wind (so-called QBO easterly phases) and westerly wind (so-called QBO westerly phases), with an averaging period of approximately 28 months (Baldwin et al., 2001). QBO is driven by vertically propagating Kelvin waves, mixed Rossby gravity waves and small-scale gravity waves (Lindzen and Holton, 1968; Holton and Lindzen, 1972; Baldwin et al., 2001; Ern et al., 2014). It could influence the transport and distribution of trace gases like water vapor and ozone in the troposphere and stratosphere (Schoeberl et al., 2008).

During the winter of 2015/16 and 2019/20, two rare stratospheric QBO disruption events occurred, which were found only twice since the record began in 1953. The events are manifested by anomalous westerly winds propagating upward, disrupting normal downward propagation of the easterly phase and producing a persistent westerly wind layer (Newman et al., 2016; Anstey et al., 2021). The 2016 QBO disruption has been confirmed to have a close causal relationship with the 2015/16 extreme El Niño event (Newman et al., 2016; Osprey et al., 2016; Barton and McCormack, 2017; Coy et al., 2017). The 2015/16 El Niño substantially weakened the subtropical easterly jet, allowing enhanced Rossby wave propagation from the extratropics into the deep tropics near 40 hPa (Barton and McCormack, 2017). These amplified Rossby waves subsequently broke and deposited momentum near the QBO westerly core, rather than at the climatological zero-wind line, causing a pronounced deceleration. The deceleration gave rise to a persistence of westerlies at 40–15 hPa, preventing the expected transition to easterlies and ultimately leading to the QBO disruption (Newman et al., 2016; Osprey et al., 2016; Coy et al., 2017; Barton and McCormack, 2017; Kang et al., 2022; Wang et al., 2023). The QBO disruption was accompanied by a marked strengthening of the Brewer–Dobson residual circulation, thereby intensifying tropical upwelling. This upwelling contributed to an upward displacement of westerlies in the tropical lower

stratosphere (Coy et al., 2017), modifying the transport and distribution of trace gases such as water vapor. The persistent westerlies also created conducive background conditions for the vertical propagation of DW1. Nevertheless, not all strong El Niño events trigger QBO disruptions. In the 2015/16 case, the QBO westerly wind core was weaker and Rossby wave activity was stronger than in other extreme events, such as the 1998 El Niño (Barton and McCormack, 2017). In the 2020 event, the upward-propagating westerly wind was so weak that the monthly mean zonal wind appeared as upward-propagating easterly wind (e.g., Anstey et al., 2021; Wang et al., 2023). This event was driven by strong extratropical Rossby waves associated with the 2019 minor SSW in the southern hemisphere (Kang and Chun, 2021; Wang et al., 2023). In these two events, the trace gases such as ozone and water vapor are modulated. During the 2016 QBO disruption event, positive water vapor anomalies were observed between the tropopause and lower stratosphere, while positive ozone anomalies appeared in the upper stratosphere (Tweedy et al., 2017; Diallo et al., 2018). A similar pattern was reported for the 2020 disruption event, with water vapor in the lower stratosphere and ozone in the upper stratosphere also exhibiting positive anomalies (Diallo et al., 2022).

QBO modulation of diurnal tides has been reported by both ground-based and space-borne observations (Araújo et al., 2017; Davis et al., 2013; Pramitha et al., 2021b; Wu et al., 2008; Dhadly et al., 2018). Mayr and Mengel (2005) reported that the QBO can affect these amplitudes by up to 30 % using the Numerical Spectral Model (NSM). Thermosphere, Ionosphere, Mesosphere Energetics and Dynamics/Sounding of the Atmosphere using Broadband Emission Radiometry (TIMED/SABER) observations revealed that the quasi-biennial variability of DW1 could exceed 50 % at certain altitudes (Garcia, 2023). The modulation was characterized by larger-than-average diurnal tide amplitudes during the westerly phase of the QBO and smaller-than-average amplitudes during the easterly phase (Vincent et al., 1998; Wu et al., 2008; Xu et al., 2009; Davis et al., 2013; de Araújo et al., 2017; Pramitha et al., 2021b; Garcia, 2023). Several mechanisms have been proposed for modulating the migrating diurnal tide (DW1). A primary factor emphasized in many studies is the variation in the background zonal wind and its latitudinal shear (Forbes and Vincent, 1989; Hagan et al., 1999; McLandress, 2002b; Riggins and Lieberman, 2013; Liu et al., 2015; Ortland, 2017; Dhadly et al., 2018; Pramitha et al., 2021a, b). Forbes and Vincent (1989) demonstrated that the DW1 (1,1) mode experiences stronger dissipation in easterly phases than in westerly phases, while McLandress (2002b) highlighted the tide's strong sensitivity to latitudinal shears in the zonal mean easterlies of the summer mesosphere. Apart from the influence of the background wind, additional contributions have been suggested, including variations in diurnal heating (McLandress, 2002b; Riggins and Lieberman, 2013; Ortland, 2017) and tide–gravity wave (GW) interactions (Mayr et al., 1998; McLandress, 2002a; Lu et al., 2012;

Wang et al., 2024), both of which may play a role in modulating the QBO-related variability of DW1.

Recent studies have shown that the diurnal tides were modulated during the QBO disruption events (Pramitha et al., 2021a; Garcia, 2023; Wang et al., 2024). Pramitha et al. (2021a) first reported the enhancement of the diurnal tides during the 2015/2016 QBO disruption event using a meteor radar over Tirupati (13.63° N, 79.4° E) and linked this enhancement to changes in ozone concentration. Garcia (2023) showed the equatorial response of temperature DW1 to these two disruption events when analysing the QBO modulation to DW1. Wang et al. (2024) reported the weakened mesospheric diurnal tides at mid-latitude during QBO disruption events, which were observed by a meteor radar chain. They further provided the modulation evidence of gravity wave forcing and solar radiative absorption by subtropical stratospheric ozone, as revealed by SD-WACCM-X simulations.

These findings raise three questions: (1) In addition to the equatorial peak, temperature DW1 exhibits secondary amplitude maxima at 30° N and 30° S (Xu et al., 2009; Garcia, 2023). Whether the DW1 amplitudes on a global scale show a similar response to the QBO disruption events. (2) Whether the phases and wavelengths of DW1 could be affected by the events. (3) Mechanisms for modulating DW1 include heating sources such as water vapor radiative heating and latent heating, zonal wind latitudinal shear, and tide–gravity wave interactions (e.g., Forbes and Vincent, 1989; Hagan, 1996; Hagan et al., 1999; McLandress, 2002a; Kogure and Liu, 2021). Whether these mechanisms play significant roles in modulating DW1 during QBO disruption events.

The present study will focus on the global response feature of DW1 and its underlying mechanisms to QBO disruption events. The response of DW1 amplitudes, phases and wavelengths during the event will be investigated. Moreover, the contribution of possible mechanisms, including heating sources, the zonal wind latitudinal shear and tidal-gravity wave interaction during the event, will be explored. The article is organized as follows: Sect. 2 introduces TIMED/SABER, SD-WACCM-X, and MERRA-2 data and the methodologies to extract the migrating tides. Section 3 presents the response feature of the DW1 to the QBO disruption events revealed by SABER/TIMED observations and SD-WACCM-X simulation results. The possible mechanism of DW1 response to the disruption events is discussed in Sect. 4. Section 5 presents the summary.

## 2 Data and methodology

This study employs the dataset of SABER/TIMED observations, SD-WACCM-X simulations and MERRA-2 reanalysis to reveal the feature of DW1 and its excitation sources during QBO disruption events. DW1 amplitude, phase, and wavelength are derived from both SABER/TIMED data and SD-WACCM-X outputs. MERRA-2 reanalysis is used to anal-

yse the contributions of water vapor radiative heating and latent heating to DW1 variability during the QBO disruption events, while SABER/TIMED observations characterize ozone radiative heating. SD-WACCM-X simulations validate the excitation source revealed by the observational datasets.

### 2.1 SABER/TIMED observations

The TIMED satellite is in a near sun-synchronous orbit with a 73° inclination at about 625 km. The number of orbits observed per day is about 15. SABER, an instrument in the TIMED satellite, is a 10-channel broadband (1.27–17  $\mu\text{m}$ ) limb-scanning infrared radiometer. SABER observations of infrared radiance are used to retrieve kinetic temperature, trace gases, etc. In this work, kinetic temperature and ozone observations in level 2A (L2A) dataset and ozone heating rate in level 2B (L2B) dataset are selected to analyse the DW1 response to QBO disruption events. Kinetic temperature is derived using a full nonlocal thermodynamic equilibrium (non-LTE) inversion algorithm (Mertens et al., 2001, 2004) with the combination of the measured 15  $\mu\text{m}$  CO<sub>2</sub> vertical emission profile and CO<sub>2</sub> concentrations provided by the Whole Atmosphere Community Climate Model (WACCM 3.5.48), as described by Garcia et al. (2007).

It takes SABER 60 d to sample 24 h in local time. The data latitudinal coverage every 60 d extends from 53° N to 83° S or 53° S–83° N. Temperature observations taken from version 2.07 data from 2002 to 2019 and version 2.08 data from 2020 to 2023 are used. The details of the version switches could refer to Mlynczak et al. (2022, 2023). The retrieved temperature observations used in this work cover altitudes from approximately 15 to 105 km.

### 2.2 SD-WACCM-X

The Whole Atmosphere Community Climate Model with thermosphere–ionosphere eXtension (WACCM-X) is a comprehensive numerical model that could simulate the Earth's atmosphere from the surface up to the upper thermosphere (~500–700 km), including the ionosphere (Liu et al., 2010, 2018). WACCM-X is a single, unified whole-atmosphere model that extends the NCAR Whole Atmosphere Community Climate Model (WACCM4; Marsh et al., 2013). WACCM4 itself was built upon the Community Atmosphere Model 4 (CAM4; Neale et al., 2010). While the thermosphere–ionosphere physics (e.g., global electrodynamics, O<sup>+</sup> transport, electron/ion energetics) incorporated in WACCM-X were largely adapted from the NCAR Thermosphere–Ionosphere–Electrodynamics General Circulation Model (TIE-GCM; Qian et al., 2014; Pedatella, 2022), they have been re-engineered within the WACCM-X dynamical core and coupled to the lower- and middle-atmosphere processes through a dedicated ionosphere-interface module. SD in the SD-WACCM-X means specified dynamics, which is an approach described in Smith et al. (2017). The reanal-

ysis fields from Modern-Era Retrospective analysis for Research and Applications, Version 2 (MERRA-2, Gelaro et al., 2017) data from the surface up to  $\sim 50$  km are nudged in WACCM-X.

Model parameters are output in 3 h resolution. The latitude-longitude resolution is  $1.9^\circ \times 2.5^\circ$ . The model has 145 pressure levels with a varying vertical resolution of  $\sim 1.1$ – $1.75$  km in the troposphere and stratosphere and  $\sim 3.5$  km in the mesosphere. In this work, the temperature, zonal wind, temperature tendency due to moist process and long wave heating rate ranging from 2002 to 2022 are selected.

### 2.3 MERRA-2

MERRA-2 is a reanalysis product from the NASA Global Modeling and Assimilation Office (GMAO) and provides data like wind, temperature, mixing ratio of components, and so on (Gelaro et al., 2017). In this work, the zonal wind, temperature, air density, surface albedo, water vapor mixing ratio and temperature tendency due to moist process range from 2002 to 2023 are selected. The time resolution is  $3 \text{ h d}^{-1}$ . The spatial resolution is a  $2.5^\circ \times 2.5^\circ$  latitude-by-longitude grid at 72 model levels from ground to 0.01 hPa.

### 2.4 Singapore radiosonde QBO index

The QBO index employed in this study is derived from Singapore radiosonde measurements obtained by the Meteorological Service Singapore Upper Air Observatory (station 48698;  $1.34^\circ \text{ N}$ ,  $103.89^\circ \text{ E}$ ; 21 m above mean sea level). The monthly mean zonal wind data processed by the National Aeronautics and Space Administration/Goddard Space Flight Center (NASA/GSFC) is selected, spanning 2002–2023 at pressure levels between 100 and 10 hPa.

### 2.5 Water vapor radiative heating rate calculation

Troposphere heating by water vapor absorption of near-infrared radiation is an important excitation source for DW1 (Hagan, 1996; Lieberman et al., 2003). Due to the SABER's observational gap in the troposphere, the MERRA-2 dataset is adopted. In this dataset, temperature, air density, surface albedo, cloud fraction and water vapor mixing ratio (specific humidity) are the variables necessary for the calculation. The heating rate is the sum of clear sky and cloudy sky (Groves, 1982):

$$J = (1 - k) J_{\text{clear}} + k J_{\text{cloudy}} \quad (1)$$

where  $k$  is the cloud fraction,  $J_{\text{clear}}$  and  $J_{\text{cloudy}}$  are the heating rates of the clear sky and cloudy sky. The calculation equations for clear sky and cloudy sky are given in Appendix A.

### 2.6 Ozone radiative heating rate calculation

The calculation of ozone radiative heating follows the Strobel/Zhu scheme (Strobel, 1978; Zhu, 1994), in which the total heating rate is obtained as the sum of contributions from the Hartley, Huggins, and Chappuis bands, with parameterizations from Zhu (1994). The required ozone volume mixing ratio (VMR) and density are taken from the SABER L2A dataset. Ozone VMR is retrieved from vertical emission profiles at  $9.6$  and  $1.27 \mu\text{m}$  (Smith et al., 2013). The former covers all local times and the latter is limited to daytime. In this study, the  $9.6 \mu\text{m}$  retrievals are used. It should be noted that the Strobel/Zhu model omits the dominant nighttime chemical-heating source between  $\sim 70$  and  $100$  km (Zhu, 1994; Xu et al., 2010). Consequently, the present analysis is restricted to the sum of the three-band heating rates between  $20$  and  $70$  km.

### 2.7 Method for extracting DW1 and data processing

Non-uniform SABER observational data were processed into zonal mean data and used to extract tides. The procedures are briefly introduced as follows. Firstly, the kinetic temperature, ozone mixing ratio and ozone radiative heating rate profiles are interpolated vertically with a  $1$  km spacing. Profiles for each day are sorted into ascending and descending groups. Secondly, the global temperature and ozone observations at whole heights and in both groups were processed into zonal mean results, covering latitudes from  $50^\circ \text{ S}$  to  $50^\circ \text{ N}$  with a resolution of  $5^\circ$ . At a fixed latitude and height, the following equation proposed by Xu et al. (2007) is used to extract the tide from the zonal mean temperature in a  $60$  d window:

$$\frac{1}{2\pi} \int_0^{2\pi} T(t_{\text{LT}}, \lambda) d\lambda = \bar{T} + \eta(t - t_0) + \sum_{n=1}^N A_n \cos(n\omega t_{\text{LT}}) + \sum_{n=1}^N B_n \sin(n\omega t_{\text{LT}}) \quad (2)$$

where  $\omega = 2\pi/24$  (hour),  $t_{\text{LT}}$  is the local time,  $\lambda$  is longitude in radians.  $\bar{T}$  is the  $60$  d window average of the zonal mean temperature.  $\eta$  describes the linear trend variation in the window.  $t$  is the day of the window and  $t_0$  is the center day of the window. The third and fourth terms of the right section of the equation denotes the superimposed harmonic signals by four periods migrating tides, including diurnal tide (DW1), semidiurnal tide (SW2), terdiurnal tide (TW3), and  $6$  h tide (QW4).  $N$  in the third term represents four signals and  $n$  denotes each signal. The amplitude and phase of each migrating tide are retrieved using  $\sqrt{A_n^2 + B_n^2}$  and  $\arctan(B_n/A_n)$ , respectively. The overlapping analyses are obtained by sliding the  $60$  d window forward in  $1$  d intervals to obtain the daily values of the wave characteristics. The details of the methods used for data processing and tide extraction could refer to Xu et al. (2007, 2009) and Liu et al. (2024a).



The method for extracting tidal components from ozone heating rates follows Eq. (4) in Xu et al. (2010). The methods for tidal extraction from MERRA-2 and SD-WACCM-X differ from those used for SABER due to differences in data structure. Unlike SABER, both MERRA-2 and SD-WACCM-X provide spatially uniform data with a 3 h temporal resolution. As a result, a two-dimensional Fast Fourier Transform (2D-FFT) is directly applied to extract daily DW1 amplitudes and phases of temperature, water vapor heating rate, and temperature tendency due to moist processes. For further analysis, the Hough mode decomposition is applied to the DW1. The program is retrieved from [https://github.com/masaru-kogure/Hough\\_Function](https://github.com/masaru-kogure/Hough_Function) (last access: 25 July 2025). As in Sakazaki et al. (2013), DW1 in the stratosphere can be reasonably well represented by a superposition of only a few ( $\sim 4$ ) Hough modes. Here the  $(1, -2)$ ,  $(1, -1)$ ,  $(1, 1)$  and  $(1, 2)$  modes are used. The monthly mean temperature DW1 amplitudes obtained from SABER, MERRA-2 and SD-WACCM-X are calculated. Due to the observational gap of SABER, the Generalized Lomb-Scargle Periodogram (from PyAstronomy) is applied to fill the missing data of ozone heating rate. A low-pass Butterworth filter of 3rd order with a cut-off period of 13 months ( $\approx 0.077$  cycles per month) is applied to reveal the DW1 QBO variations (temperature, ozone heating and so on).

### 3 Result

#### 3.1 DW1 amplitude response to QBO disruption events

Figure 1 presents the amplitude of DW1 after low-pass filtering and the zonal wind observed by the Singapore sonde. Only amplitude components with periods longer than 13 months are retained. In the stratosphere, the zonal wind shows alternating downward propagating westerly wind (positive value in Fig. 1e and f) and easterly wind (negative value in Fig. 1e and f). Each westerly and easterly transition can be called a QBO cycle. In the stratosphere (Fig. 1c and d), below 40 km, the amplitude of DW1 also shows Quasi-Biennial variability. Above 40 km, the variation becomes more complex. This feature will be discussed later. In the MLT region (Fig. 1a and b), the low-pass filtering results of DW1 at the equator exhibit Quasi-Biennial variability, with amplitude peaks observed around 90 and 100 km. Comparing the DW1 amplitudes in MLT with the zonal wind, the result reveals that the variations in DW1 amplitude correspond to the zonal wind between 20 and 30 hPa. The amplitude of DW1 is stronger during the QBO westerly wind phase than during the QBO easterly wind phase. This result is consistent with Garcia (2023) that the wind fields of QBO at altitudes below 27 km are clearly correlated with the DW1 amplitude. Accordingly, in this work, the zonal wind between 20 and 30 hPa is used as the criterion for defining the QBO for DW1.

During February–May 2016 and January–May 2020, two QBO disruption events occurred (Wang et al., 2023). As

shown in Fig. 1f, the phenomenon ranges from 40 to 15 hPa in 2016 and from 40 to 20 hPa in 2020, which is consistent with previous work (Anstey et al., 2021; Newman et al., 2016). Notably, the disruption region coincides with the QBO criterion altitude for DW1. To evaluate how the DW1 exhibits responses to the events, the corresponding time intervals are highlighted with vertical green dashed lines. In the stratosphere (Fig. 1d), within the disruption periods, amplitude enhancements are observed below 40 km compared to other QBO easterly phases. Similarly, in the MLT region, the DW1 amplitudes show responses to these events (Fig. 1b). As shown in Fig. 1a and b, DW1 amplitudes above 70 km are stronger during these disruption events than during other QBO easterly phases, though they remain weaker than those observed during the QBO westerly phase. This enhancement is particularly evident around 90 and 100 km.

SD-WACCM-X simulations reproduce the SABER observations of DW1 remarkably well in response to QBO disruptions. In Fig. 1a, b, f, and g, both datasets show enhanced amplitudes during the February–May 2016 and January–May 2020 events. The difference arises in vertical structure and magnitude. Above 70 km, SABER exhibits three distinct DW1 peaks near 80, 90, and 100 km, whereas SD-WACCM-X shows a single peak at approximately 108 km. In the stratosphere above 40 km, both model and observations peak at similar altitudes, but the simulated amplitudes remain weaker than SABER result. Below 40 km, the model captures the QBO-modulated DW1 seen in Fig. 1c, d, i, and j. These discrepancies likely stem from the MERRA-2 nudging applied up to  $\sim 50$  km in SD-WACCM-X. In this nudged region, DW1 comprises both propagating and non-propagating components (Garcia, 2023; Chapman and Lindzen, 1970). Sakazaki et al. (2018) showed that MERRA-2 may underestimate the contribution of the non-propagation mode of DW1 (Fig. 4 in that work). This feature may explain why the amplitude of DW1 is lower than that in SABER and the complex variation of SABER above 40 km.

To assess the DW1 response to QBO disruption events over a broad latitude range, the differences between QBO disruption and regular QBO easterly and westerly phases are calculated. The DW1 amplitudes used are the result after 13 months low-pass filtering. Since the DW1 amplitudes typically peak between February and April each year (e.g., Xu et al., 2009; Mukhtarov et al., 2009; Garcia, 2023), only the amplitudes during these three months are considered. The classification method for different QBO phases is as follows. Regular QBO phases were classified using the following method. QBO westerly phase (QBOW): February–April zonal wind at 20 hPa is continuously westerly, or zonal wind at 30 hPa is westerly while 20 hPa undergoes an easterly-to-westerly transition. Easterly phase (QBOE): any remaining cases. The selection of regular QBO phases is limited to data from 2002 to 2014, as QBO disruption events occurred after 2015. Additionally, since observations in 2002 are mainly available from March to April, data from this year are ex-

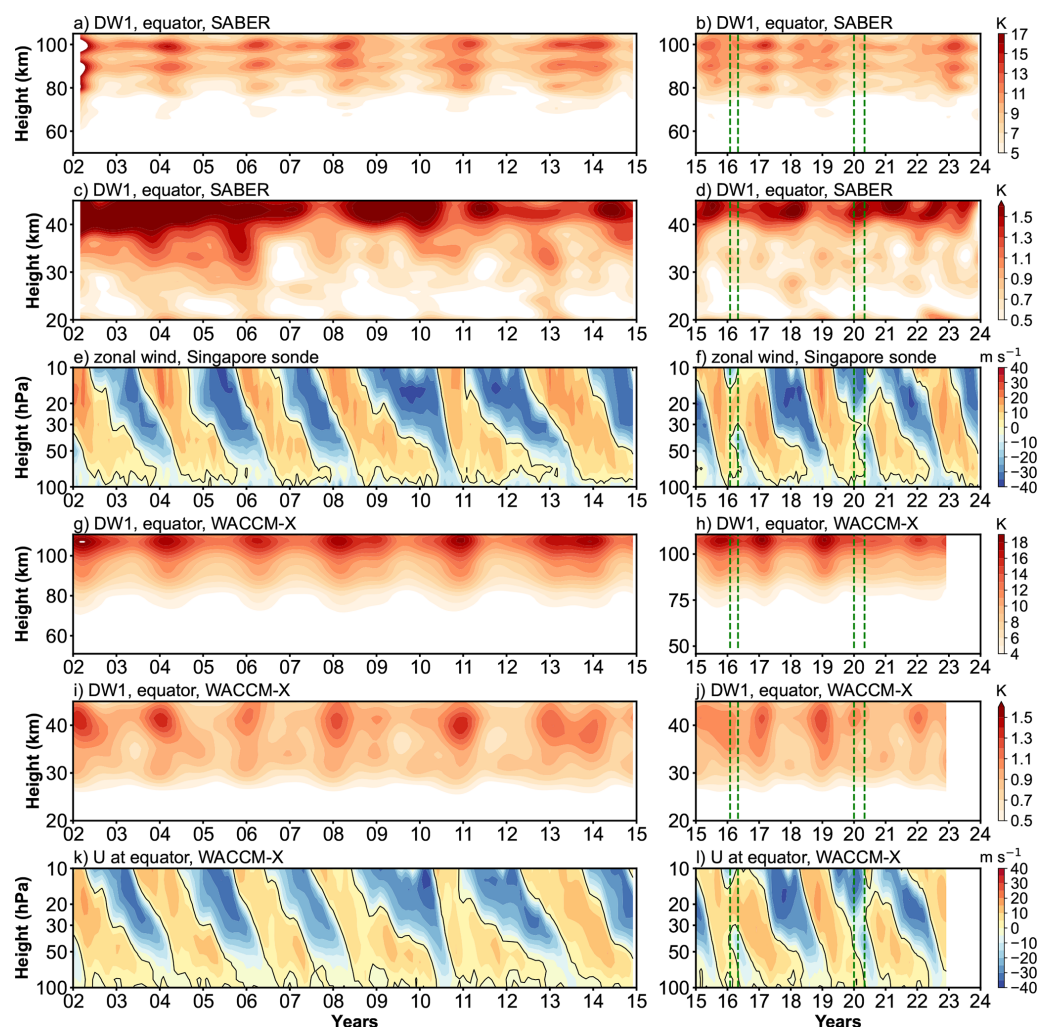


**Figure 1.** (a, b) Low-pass filtered amplitudes (periods longer than 13 months) of the migrating diurnal tide (DW1; monthly mean, in K) as a function of altitude in the mesosphere and lower thermosphere (MLT) and time (2002–2023), derived from SABER/TIMED temperature observations. (c, d) Same as panels (a) and (b) but for the stratosphere. (e, f) Zonal wind at the stratospheric equator from Singapore sonde. (g–i) Similar to panels (a)–(f), but based on SD-WACCM-X simulations. Vertical green dashed lines indicate the QBO disruption periods in 2015/16 (February–May 2016) and 2019/20 (January–May 2020).

cluded. The years 2004, 2006, 2008, 2011, 2013, and 2014 are classified as QBOW; 2003, 2005, 2007, 2009, 2010, and 2012 as QBOE. For each phase, all filtered amplitudes across the selected months are averaged, while processing data for 2016 and 2020 separately. This approach enables a direct comparison of DW1 amplitude anomalies in both latitude and altitude between disruption and regular QBO conditions.

Figure 2 gives the difference in DW1 amplitudes during various QBO phases in the MLT region. The significance of the differences was assessed using Welch's *t*-test, and values exceeding the 95 % confidence threshold are highlighted in dotted. The five columns correspond to the 2016 disruption event minus QBO westerly (2016 – QBOW), 2020 disruption event minus QBO westerly (2020 – QBOW), QBO westerly minus QBO easterly (QBOW – QBOE), 2016 disruption event minus QBO easterly (2016 – QBOE) and 2020 disruption event minus QBO easterly (2020 – QBOE), respectively. The relative change between different QBO phases is also calculated (e.g.,  $\frac{\text{QBOW} - \text{QBOE}}{\text{QBOE}}$ , and so on). The comparison between QBOW and QBOE (Fig. 2c) reveals that DW1 amplitudes are significantly larger during QBOW, particularly at the equator and around 30° N/S above ~ 75 km. The enhancements reach ~ 2.79 K (~ 34.5 %) at the equator and ~ 0.79 K (~ 20.6 %) at 30° N/S, with peak values as high as ~ 3.30 K (~ 38.5 %) and ~ 1.19 K (~ 31.7 %) at respective latitudes. During the 2016 disruption (Fig. 2a, d), DW1 amplitudes lie between QBOE and QBOW values. The clear enhancement could be found from 75 to 105 km. The pattern in 2016 – QBOE closely resembles that of QBOW – QBOE, although the

(QBOW – QBOE), 2016 disruption event minus QBO easterly (2016 – QBOE) and 2020 disruption event minus QBO easterly (2020 – QBOE), respectively. The relative change between different QBO phases is also calculated (e.g.,  $\frac{\text{QBOW} - \text{QBOE}}{\text{QBOE}}$ , and so on). The comparison between QBOW and QBOE (Fig. 2c) reveals that DW1 amplitudes are significantly larger during QBOW, particularly at the equator and around 30° N/S above ~ 75 km. The enhancements reach ~ 2.79 K (~ 34.5 %) at the equator and ~ 0.79 K (~ 20.6 %) at 30° N/S, with peak values as high as ~ 3.30 K (~ 38.5 %) and ~ 1.19 K (~ 31.7 %) at respective latitudes. During the 2016 disruption (Fig. 2a, d), DW1 amplitudes lie between QBOE and QBOW values. The clear enhancement could be found from 75 to 105 km. The pattern in 2016 – QBOE closely resembles that of QBOW – QBOE, although the

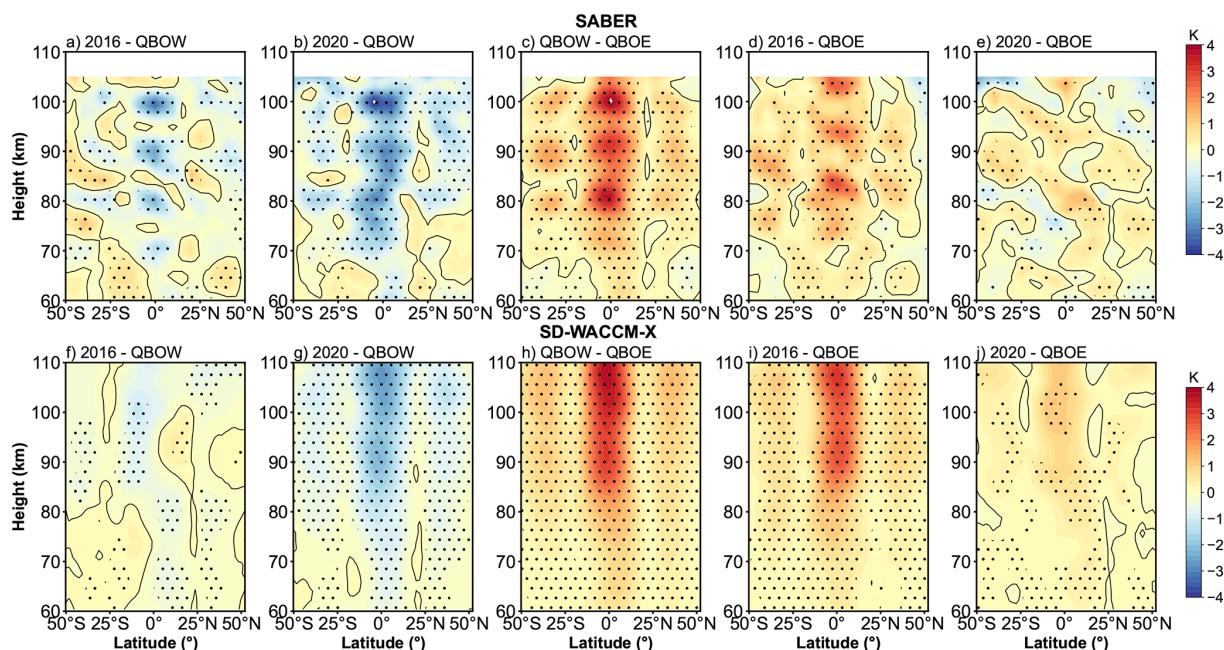


**Figure 2.** Amplitude differences of the DW1 after low-pass filtering between different QBO phases in the mesosphere and lower thermosphere (MLT) as a function of latitude and altitude. The difference is based on the average from February to April. Panels (a)–(e) are corresponding to the difference from the 2016 disruption event minus QBO westerly phases (2016 – QBOW), 2020 disruption event minus QBO westerly (2020 – QBOW), QBO westerly minus QBO easterly (QBOW – QBOE), 2016 disruption event minus QBO easterly (2016 – QBOE) and 2020 disruption event minus QBO easterly (2020 – QBOE). Panels (f)–(j) are similar to panels (a)–(e) but for SD-WACCM-X simulation result. The black lines indicate the zero lines. The dotted areas indicate the differences that are significant at the 95 % confidence level.

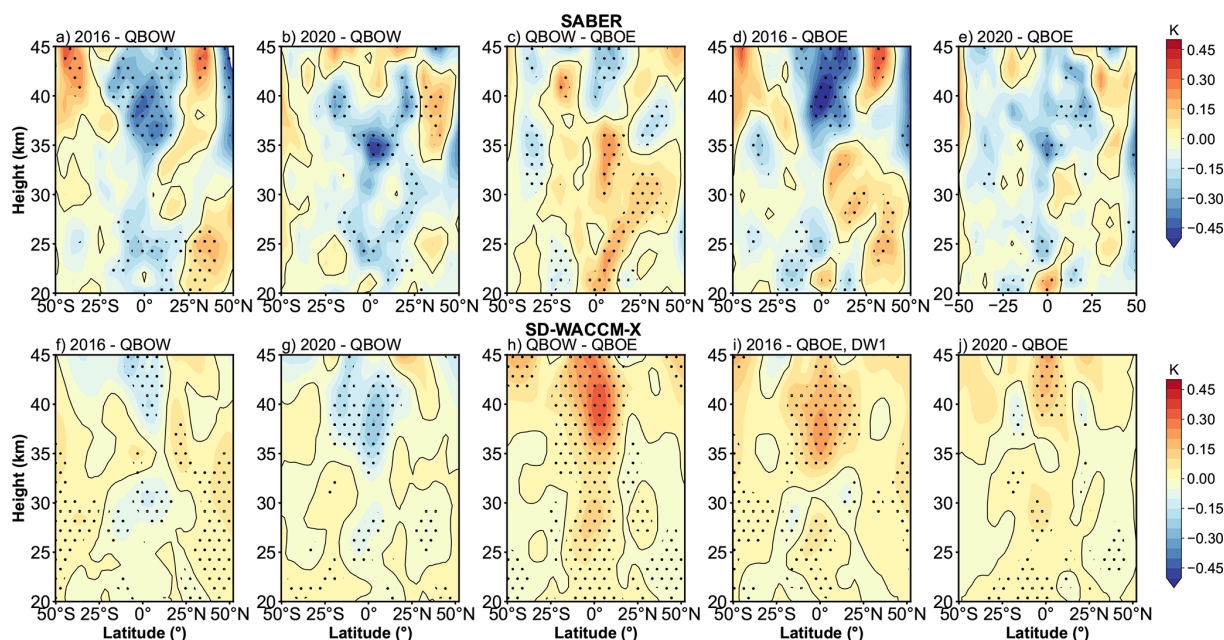
equatorial peaks appear at slightly higher altitudes. The enhancements reach  $\sim 1.56$  K ( $\sim 20.5$  %) at the equator and  $\sim 0.54$  K ( $\sim 14.4$  %) at  $30^\circ$  N/S. The peak enhancements relative to QBOE reach  $\sim 2.40$  K ( $\sim 26.5$  %) at the equator and  $\sim 0.87$  K ( $\sim 29.5$  %) at  $30^\circ$  N/S. Compared to QBOW, however, the difference drops to  $-2.28$  K ( $-18.8$  %) at equator and  $\sim 0.12$  K (4.6 %) at  $30^\circ$  N/S. In contrast, the 2020 disruption event shows weaker amplitude increases relative to QBOE (Fig. 2b, e). The clear enhancement occurs from 75 km to 90 km. The increment reaches  $\sim 0.50$  K ( $\sim 6.0$  %) at the equator and  $\sim 0.26$  K ( $\sim 7.7$  %) at  $30^\circ$  N/S, with a peak enhancement of only  $\sim 0.91$  K ( $\sim 11.6$  %) at the equator and  $\sim 0.31$  K ( $\sim 14.2$  %) at  $30^\circ$  N/S. Compared to QBOW, the difference is  $-2.3$  K ( $\sim -21.1$  %) at the equator and  $-0.57$  K ( $\sim -12.0$  %) at  $30^\circ$  N/S. These values are considerably lower than those observed during the 2016 event or the typical QBOW enhancement. The SD-WACCM-X model reproduces the general features described above (Fig. 2f–j), though the vertical structure of the simulated amplitudes differs slightly from observations.

Figure 3 compares the stratospheric DW1 amplitude differences derived from the SABER dataset and SD-WACCM-X simulations. The enhancement pattern resembles that seen in the MLT region but is confined to tropical latitudes. Because SABER exhibits complex variability above 40 km, the

analysis is restricted to altitudes below that level. As shown in Fig. 3c, the DW1 amplitudes during QBOW exceed those during the QBOE by  $\sim 0.21$  K ( $\sim 37.9$  %) at around 20–25 and 30–35 km. In SD-WACCM-X result (Fig. 3h), the positive peaks are found at 25–30 and 35–40 km, which is  $\sim 0.21$  K ( $\sim 27.4$  %). The amplitudes during the disruption events are much weaker relative to those during QBOW phases shown in both datasets (Fig. 3a, b, f and g). Compared to QBOE, the strengthening during the 2016 QBO disruption event occurs at approximately 30–35 km in SABER (Fig. 3d) and 35–45 km in SD-WACCM-X (Fig. 3i), which is  $\sim 0.15$  K ( $\sim 21.8$  %) and  $0.20$  K ( $\sim 23.9$  %), respectively. During the 2020 event, the amplitudes are comparable to those during QBOE (Fig. 3e and j).

Figure C2 presents the low-pass time series of the equatorial DW1 amplitude and the (1, 1) mode amplitude at 95 km, showing that the (1, 1) mode closely follows the equatorial DW1 amplitude. In the stratosphere, however, the superposition of propagating tides and trapped modes complicates the interpretation. To separate these contributions, Fig. C1 compares the amplitudes of the (1, 1) and (1, –2) modes under different QBO phases. The trapped mode is dominant below 60 km, while the (1, 1) mode is relatively weaker. A clear distinction between QBOW and QBOE is evident in the (1, 1) mode (Fig. C1a), whereas the (1, –2) mode shows little





**Figure 3.** Similar to Fig. 2 but in stratosphere. Panels (a)–(e) give the difference result derived from SABER. Panels (f)–(j) give the difference result derived from SD-WACCM-X.

difference between the phases. Together, Figs. C1 and C2 indicate that the (1, 1) mode captures nearly all of the QBO-related variability in the MLT region, motivating a closer examination of the (1, 1) mode in the stratosphere.

Figure 4 shows the vertical profiles of amplitude differences in the DW1 (1, 1) mode between QBO phases after low-pass filtering. The bold lines denote differences significant at the 95 % confidence level. In SABER observations (Fig. 4a), amplitudes during QBOW exceed those in QBOE throughout 20–45 km. During the 2016 and 2020 events, amplitudes remain close to those in QBOE between 20–40 km but become stronger above 40 km, with maximum differences of  $\sim -0.15$  ( $\sim -11\%$ ),  $-0.18$  ( $\sim -12\%$ ),  $\sim 0.36$  K ( $\sim 36\%$ ),  $\sim 0.21$  K ( $\sim 21\%$ ), and  $\sim 0.18$  K ( $\sim 17\%$ ) for 2016 – QBOW, 2020 – QBOW, QBOW – QBOE, 2016 – QBOE, and 2020 – QBOE, respectively. WACCM-X simulations (Fig. 4b) reproduce a similar vertical pattern: during the disruption events, amplitudes lie between QBOE and QBOW values in the 20–50 km region.

### 3.2 DW1 phases response to QBO disruption events

In this section, whether the DW1 phases and wavelengths respond to QBO disruptions will be analysed. As discussed above, the DW1 QBO variability is mainly in (1, 1) mode. Hence, we focus on the phase of (1, 1) mode. As noted previously, the pronounced DW1 amplitude observed from February to April renders the phase during this period an important variable. Hence, the statistics are based on these periods. Since the phase values change cyclically (e.g., it jumps

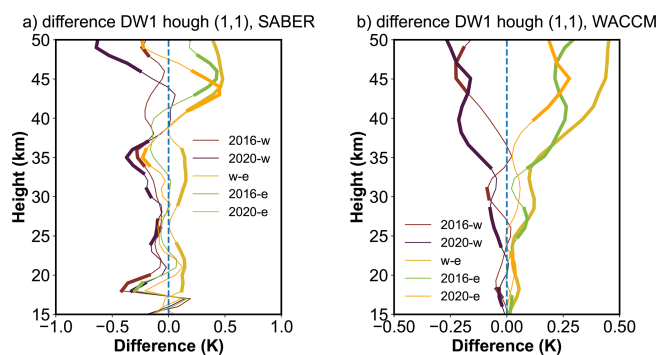


**Figure 4.** Amplitude differences profiles of the DW1 (1, 1) mode after low-pass filtering between different QBO phases in the stratosphere like Fig. 2. Panel (a) gives the difference result derived from SABER. Panel (b) gives the difference result derived from SD-WACCM-X. The bold lines indicate the differences that are significant at the 95 % confidence level.

from  $\pi$  to  $-\pi$ ), causing the overestimation of the standard deviation. We apply the following method. We first calculate averages and standard deviation (or error) of sine and cosine Fourier components, and then calculate the average phase and its confidence interval using error propagation. The mean value and its 95 % confidence interval in different QBO phases (listed in Sect. 3.1) are calculated. The statistical results for the phases in 2016 and 2020 are calculated separately.

Figure 5 illustrates the vertical phase structure of DW1 (1, 1) mode in the mesosphere and lower thermosphere (MLT)



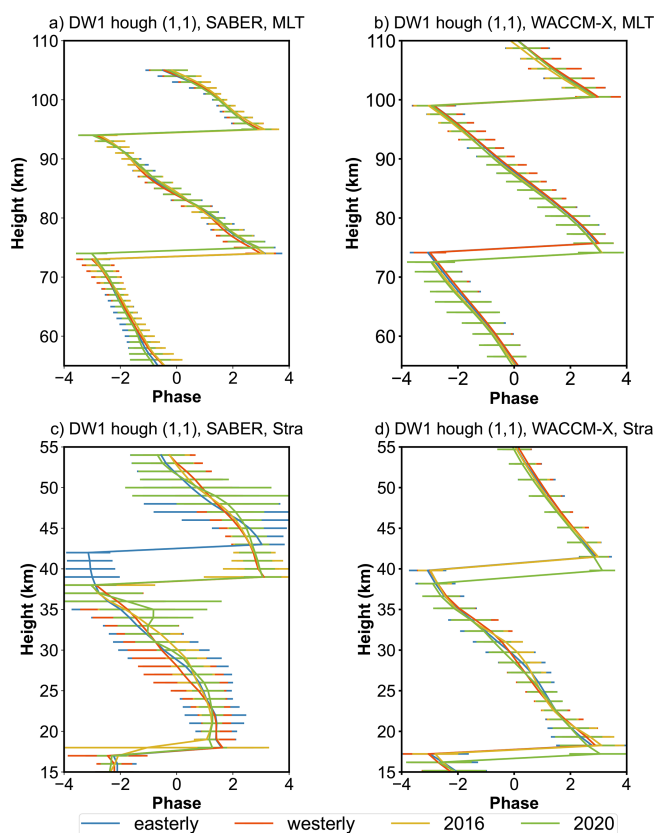


**Figure 5.** The DW1 (1, 1) mode vertical phase structure in mesosphere and lower thermosphere (MLT) and stratosphere averaged from February to April during QBO westerly phase (orange), QBO easterly phase (blue), 2016 QBO disruption event (yellow) and 2020 QBO disruption event (green). Panels (a) and (c) give the SABER observation result. Panels (b) and (d) give the WACCM-X simulations. The error bar denotes the 95 % confidence interval of the phases for each height.

and stratospheric regions, respectively, averaged over the February–April period. The results are presented for various QBO phases at different latitudes, based on data from (Fig. 5a, c) SABER and (Fig. 5b, d) SD-WACCM-X. Error bars indicate the 95 % confidence interval of the phase average. The lines represent different QBO phases and events: QBO westerly phase (orange), QBO easterly phase (blue), the 2016 QBO disruption event (yellow), and the 2020 QBO disruption event (green).

In the MLT region (Fig. 5a and b), the vertical phase profiles exhibit minimal differences across the QBO westerly, easterly and 2016 phases. The structures are nearly identical in both the simulations and observations, with two phase peaks (approximately  $\pi$  rad) consistently present. The peak altitudes remain almost unchanged among the different QBO phases, suggesting a limited phase response to QBO disruption events in the MLT region. During the 2020 event, the phase peaks at around 75 km is higher than that during other QBO phases in SABER and lower than that in WACCM-X.

The DW1 vertical phase structures in the stratosphere region are given in Fig. 5c and d. In SABER observations, there are clear differences between QBOW and QBOE. The phase peaks (at around 40 km) during the QBOW occur about 3 km lower than those during QBOE. During the QBO disruption events, the phase structure is similar to that during the QBOW. From WACCM-X simulations, the feature is similar to the pattern in MLT (Fig. 5b). During the 2020 disruption event, the phase peaks are lower than other QBO phases by about 1 km.

The phase peaks described above ( $\sim \pi$  rad) are used to calculate the DW1 wavelengths in both the stratosphere and MLT regions. The altitude difference between the two peaks is taken as the wavelength, following the method of Liu et al. (2021). The statistical results of DW1 (1, 1) mode wavelengths under different QBO phases are summarized in Table 1, which lists the mean values and standard deviations at various altitudes. In the MLT region, the mean wavelengths are  $\sim 21$  km in the SABER dataset and  $\sim 25$  km in the SD-WACCM-X dataset. The wavelengths during QBO disruption events are comparable to those during the QBO westerly and easterly phases, a feature also captured in the SD-WACCM-X simulations. In the mesosphere, the mean wavelengths are  $\sim 34$  km in SD-WACCM-X and  $\sim 33$  km in SABER. In this region, there are clear differences between QBOW and QBOE. The QBOE wavelength is about 2 km shorter than that during QBOW. In the stratosphere, the QBOE wavelength is about 2 km longer than that during QBOW. The wavelengths during the QBO disruptions are close to those during QBOW.

According to the theoretical framework proposed by Forbes and Vincent (1989) and Kogure and Liu (2021), zonal winds modify the intrinsic frequency of tides through Doppler shifting, thereby altering their vertical wavelengths. Specifically, westerly winds lead to longer DW1 vertical wavelengths, whereas easterly winds result in shorter ones. However, the dependence shown in Table 1 differs from that reported in previous studies. This discrepancy can be attributed to differences in methodology. In this study, the vertical wavelengths are determined from the phase difference between adjacent peaks ( $+\pi$ ). In the stratosphere, one of these peaks typically occurs in the lower stratosphere ( $\sim 18$  km) and the other in the upper stratosphere ( $\sim 40$  km). Consequently, the estimated wavelengths encompass the combined influences of both the QBO and SAO, producing a mixed result that deviates from earlier findings.

## 4 Discussion

In this section, we discuss how the QBO disruptions modulate the DW1 by several mechanisms from the lower atmosphere to the upper atmosphere. As in Introduction, three primary mechanisms are considered: background zonal wind and its latitudinal shear (e.g., Forbes and Vincent, 1989;

**Table 1.** The comparison of mean (left of the slash) and standard deviations (right of the slash) of DW1 (1, 1) mode wavelengths (in km) revealed by SD-WACCM-X and SABER from 15 to 105 km between QBO westerly phase, easterly phase, 2016 disruption event and 2020 disruption event calculated from February to April.

Data	SD-WACCM-X			SABER		
altitude	~ 15–~ 40 km	~ 40–~ 75 km	~ 75–~ 105 km	~ 15–~ 40 km	~ 40–~ 75 km	~ 75–~ 105 km
Westerly	22.97/1.49	34.47/1.79	25.10/1.84	21.81/1.44	33.12/1.78	21.29/1.04
Easterly	22.51/1.73	34.42/2.15	25.60/2.20	24.46/1.99	30.84/2.35	20.56/1.30
2016	22.56/1/33	33.26/1.58	25.58/2.03	21.48/2.31	33.32/2.10	21.28/0.85
2020	22.71/1.87	33.80/2.68	26.27/2.41	21.08/1.77	34.24/1.46	20.39/1.35

Hagan et al., 1999; McLandress, 2002b); diurnal heating (McLandress, 2002b; Riggins and Lieberman, 2013; Ortland, 2017); tide–gravity wave (GW) interactions (Mayr et al., 1998; McLandress, 2002a; Lu et al., 2012; Wang et al., 2024). The mechanism analysis will be organized by tidal heating (troposphere and stratosphere), the dissipation and tidal propagation (from stratosphere to mesosphere) and tide–gravity wave interaction (mesosphere and lower thermosphere).

#### 4.1 Tidal heating variation during the QBO disruption events

The excitation sources of DW1 can be broadly classified into three categories: (1) solar radiation in the near-infrared (IR) absorbed by tropospheric H<sub>2</sub>O, (2) solar radiation in the ultraviolet (UV) absorbed by stratospheric and lower mesospheric O<sub>3</sub>, and (3) solar radiation absorbed by O<sub>2</sub> in the Schumann–Runge bands and continuum (Hagan, 1996). Additionally, Kogure and Liu (2021) highlighted the role of latent heating in modulating DW1. It is worth noting that the timing of the 2016 QBO disruption event coincides with the phase of the extreme El Niño (e.g., Santoso et al., 2017; Hu and Fedorov, 2017). El Niño itself could modulate the DW1 (Kogure and Liu, 2021). Attention should be paid to the contribution of water vapor and latent heating jointly influenced by QBO disruption and 2015/16 extreme El Niño. Overall, this section focuses on examining the effects of water vapor radiative heating, ozone radiative heating, and latent heating on DW1.

Figure 6 presents the difference of amplitude in the DW1 component of water vapor radiative heating rate, ozone radiative heating rate, and longwave heating rate. The calculation method is consistent with the method described in Sect. 3.1. During QBOE and QBOW, the DW1 component of water vapor heating remains nearly unchanged (Fig. 6c). However, during the 2016 QBO disruption (Fig. 6a, d), a notable enhancement in water vapor heating appears between 10–13 km altitude around the equator. The difference between 2016 and QBOE is  $\sim 0.02 \text{ K d}^{-1}$  with increases of  $\sim 2.5 \%$  relative to QBOW. The difference between 2016 and QBOW is  $0.03 \text{ K d}^{-1}$  with increases of  $\sim 3.7 \%$  relative to QBOW. A

similar pattern is seen during the 2020 QBO disruption event (Fig. 6b and e). The relative changes of the regional average increase by  $\sim 1.2 \%$  compared to QBOW and  $\sim 2.3 \%$  compared to QBOE.

Figure 6f–j reveal that the largest QBO-related differences in the DW1 component of ozone heating occur near the equator between 30 and 45 km. In QBOW, ozone heating rates between 35 and 45 km exceed those in QBOE by  $\sim 2.1 \%$  (Fig. 6h). During the 2016 QBO disruption event (Fig. 6f and i), ozone radiative heating rates are  $\sim 3.6 \%$  larger than those in the QBOW between 30 and 35 km and  $\sim 2.9 \%$  larger than those in the QBOE within the 30–40 km range. In contrast, during the 2020 disruption event (Fig. 6g and j), the ozone heating rate is comparable to that of the easterly phase and lower than that of the westerly phase in the 35–45 km altitude range.

In the SD-WACCM-X simulation, the longwave heating rate accounts for the effects of three major absorbers: H<sub>2</sub>O, CO<sub>2</sub>, and O<sub>3</sub> (Neale et al., 2010). This parameter could be used to verify the effect of the water vapor and ozone radiative heating. The DW1 component of the longwave heating rate from SD-WACCM-X is shown in Fig. 6k–o. The heating rate difference between the QBOW and QBOE reveals a positive peak at 40 km near the equator, with no significant difference at the equatorial tropopause (Fig. 6m). The feature corresponds to the observed pattern (Fig. 6c and h). In the 2016 disruption case, the simulated equatorial heating rate exhibits positive peaks around 35 and 15 km (not significant), aligning well with observations in terms of altitude (Fig. 6k and n). In the 2020 disruption case, the simulation (Fig. 6l and o) agrees with the observed stratospheric heating features (Fig. 6g and j). However, at around 15 km, the simulation shows negative peaks near the tropopause, whereas the observations indicate positive peaks (Fig. 6b and e). As longwave heating incorporates contributions from multiple absorbers, the discrepancies may be attributed to the influence of other constituents.

As discussed above, the (1, 1) Hough mode captures nearly all QBO-related variability in the MLT. Accordingly, the (1, 1) component of the ozone heating rate is extracted for diagnosis. Numerous studies have noted that the vertical thickness of ozone heating ( $\sim 40 \text{ km}$ ) is large compared with

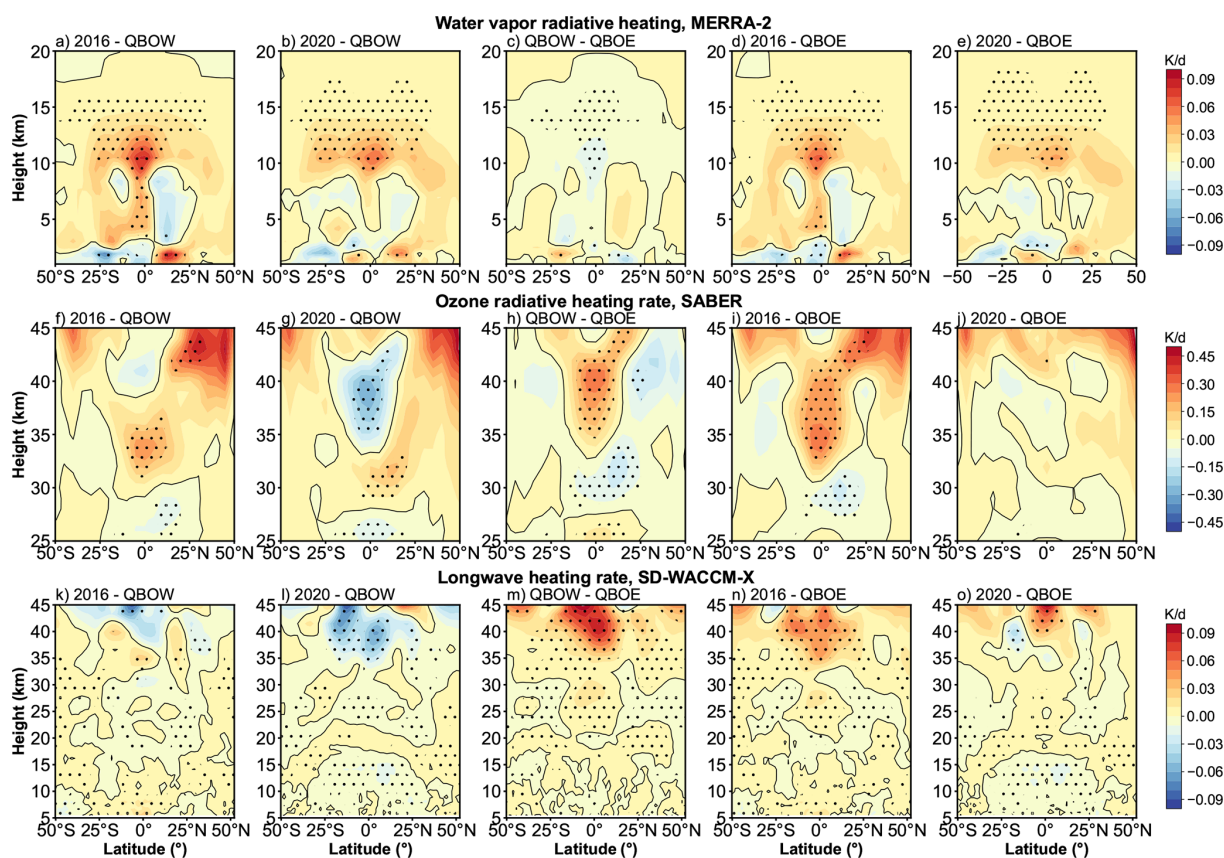


**Figure 6.** As in Figs. 2 and 3, but the difference of amplitude in DW1 component (after low-filtering) of (a–e) water vapor heating rate DW1 component from MERRA-2, (f–j) ozone heating rate DW1 component from SABER and (k–o) longwave heating rate from SD-WACCM-X. The dotted areas indicate the differences that are significant at the 95 % confidence level.

the relatively short vertical wavelength of the DW1, implying weak projection onto the (1, 1) and thus limited excitation efficiency (e.g., Chapman and Lindzen, 1970; Hagan et al., 1999; Garcia, 2023). Studies with GSWM and the Tide Mean Assimilation Technique (TAMT) further indicate that DW1 forced by ozone heating tends to be out of phase with DW1 forced by water-vapor heating, reducing the amplitudes (Hagan, 1996; Ortland, 2017). Consistent with this mechanism, MLS observations show a pronounced depression of the tropical diurnal tide near 1.0 hPa ( $\sim 49.5$  km; Wu et al., 1998), which may be attributed to interference between the upward-propagating (1, 1) tide and a locally forced component from ozone heating. Figure 7 compares DW1 (1, 1) temperature and ozone heating rate between different QBO phases and shows a suppressed (1, 1) amplitudes feature around  $\sim 50$  km, while ozone heating peaks slightly below this level. This feature aligns with the MLS evidence. Therefore, the ozone may not play a positive role for the DW1 (1, 1) mode. Whether ozone heating modulated DW1 (1, 1) mode requires more detailed investigation like model simulation from Kogure et al. (2023).

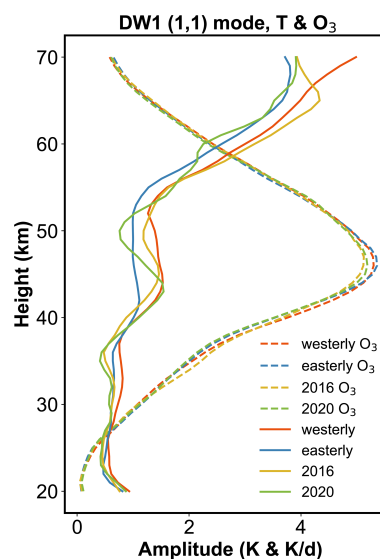


**Figure 7.** The comparison between the temperature and heating rate of the DW1 (1, 1) mode between different QBO phases.



The DW1 (1, 1) mode is primarily excited by water-vapor heating (Forbes and Garrett, 1978). As shown in Eqs. (A1) and (A10) in Appendix A, the concentration of water vapor is one of the key factors controlling water vapor radiation. During the 2016 QBO disruption, which coincided with the strong 2015/2016 El Niño, the two phenomena jointly modulated the DW1 water vapor heating sources. El Niño enhances moisture anomalies that increase with altitude, culminating in pronounced positive signals in the upper troposphere and lower stratosphere (UTLS) (Johnston et al., 2022). In contrast, the occurrence of the 2016 QBO disruption introduces a shear transition from westerly to easterly near 40 hPa, which strengthens tropical upwelling and lowers cold-point temperatures. This dynamical response injects H<sub>2</sub>O-poor air into the lower stratosphere, partially offsetting the El Niño-driven moistening. The water vapor concentrations remain above the climatological seasonal cycle under the modulation of these two phenomena (Diallo et al., 2018). Unlike 2016, the 2020 disruption produces only weak lower-stratospheric dehydration ( $\sim 2\%$ – $3\%$ ) because enhanced upwelling and cold-point cooling are suppressed. Instead, anomalously warm tropopause temperatures associated with Australian wildfire smoke facilitate significant moistening of the lower stratosphere (Diallo et al., 2022). It is foreseeable that the increase in water vapor concentration modulated by QBO disruptions and 2015/16 El Niño event will lead to an increase in the radiative heating rate of water vapor.

Figure 8 presents the water vapor radiative heating rate profiles of the DW1 (1, 1) mode for different QBO phases and their differences. The heating rate exhibits large values in the troposphere, extending up to  $\sim 10$  km. The average magnitude could reach  $\sim 0.62 \text{ K d}^{-1}$ . During the 2016 QBO disruption event (Fig. 8b), the maximum difference occurs at 10.5 km, reaching  $0.043 \text{ K d}^{-1}$ , which represents an  $\sim 8\%$  increase relative to QBOE. However, the DW1 amplitude varies by  $\sim 20.5\%$  compared to QBOE, indicating that water-vapor heating accounts for only  $\sim 39\%$  of the observed amplitude difference. This feature suggests that additional mechanisms must be involved. A similar enhancement of water-vapor heating is observed during the 2020 event, with the largest difference again at 10.5 km ( $\sim 0.026 \text{ K d}^{-1}$ ), corresponding to an  $\sim 5\%$  increase relative to QBOE.

Figure 9 shows the deseasonalized time series of the DW1 component of latent heating rate ( $\text{K d}^{-1}$ ) at the equator, averaged from 800 to 200 hPa. In this tropospheric layer, the latent-heating signal shows less differences between QBOW and QBOE phases. Therefore, deseasonalization is directly applied to the full time series without separating the two QBO states. In MERRA-2 and SD-WACCM-X, the anomaly peaks reach 0.162 and  $0.037 \text{ K d}^{-1}$ , respectively, which correspond to increases of about  $\sim 32\%$  and  $\sim 25\%$  above their climatological means ( $0.50$  and  $0.15 \text{ K d}^{-1}$ ). When averaged over February–April in 2016, the anomalies remain elevated at  $0.11 \text{ K d}^{-1}$  ( $\sim 22\%$ ) in MERRA-2 and  $0.03 \text{ K d}^{-1}$

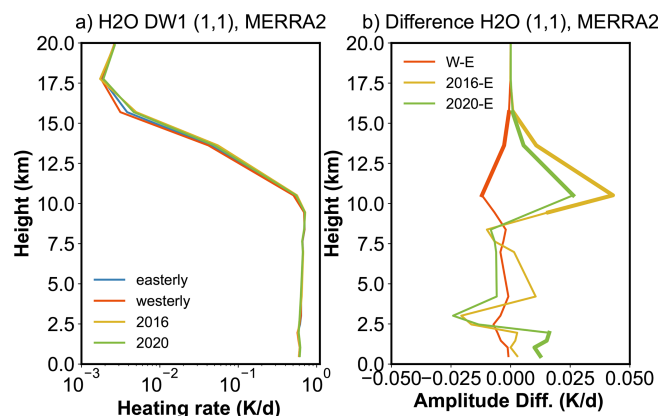


**Figure 8.** Heating rate profiles of the DW1 (1, 1) mode between different QBO phases and their differences. Panels (a) and (b) give the water vapor heating profile and its difference derived from MERRA2. The bold lines indicate the differences that are significant at the 95 % confidence level.

( $\sim 19.2\%$ ) in SD-WACCM-X. In contrast, during the 2020 QBO disruption event, the amplitudes in both MERRA-2 and SD-WACCM-X remain closer to the climatological means, with deviations of  $0.018$  and  $-0.013 \text{ K d}^{-1}$ , respectively. These results suggest that latent heating may contribute to the amplification of DW1 amplitudes during the 2016 QBO disruption event but show little effect during the 2020 event.

#### 4.2 Effect of zonal wind and its latitude shear during the events

In this section, we focus on the effects of the background wind on tides during their upward propagation. As discussed in Forbes and Vincent (1989), zonal winds distort the tidal expansion functions such that they are amplified and broadened in the winter hemisphere ( $U > 0$ ) but are considerably diminished under summer conditions. As shown in Fig. 1f, during the 2016 QBO disruption, the westerly wind layer is unusually thick in the stratosphere, though still weaker than in the normal QBOW. In contrast, during the 2020 event, the westerly wind layer is extremely shallow, essentially indistinguishable from the easterly phase. Thus, the zonal wind in the stratosphere during the 2016 QBO disruption is conducive to the growth of tidal amplitude. During the 2020 QBO disruption event, the influence of zonal winds in the stratosphere on tides is essentially consistent with that observed during the QBOE period.

Additionally, the zonal wind influences the intrinsic frequency through Doppler shifting and therefore modifies the variation of the vertical wavenumber. The increase or decrease of the vertical wavenumber depends on the direction of zonal wind. Under the usual Newton-cooling/Rayleigh-friction parameterizations, the effective dissipation is approximately proportional to the squared local vertical wavenumber (Forbes and Vincent, 1989; Kogure and Liu,



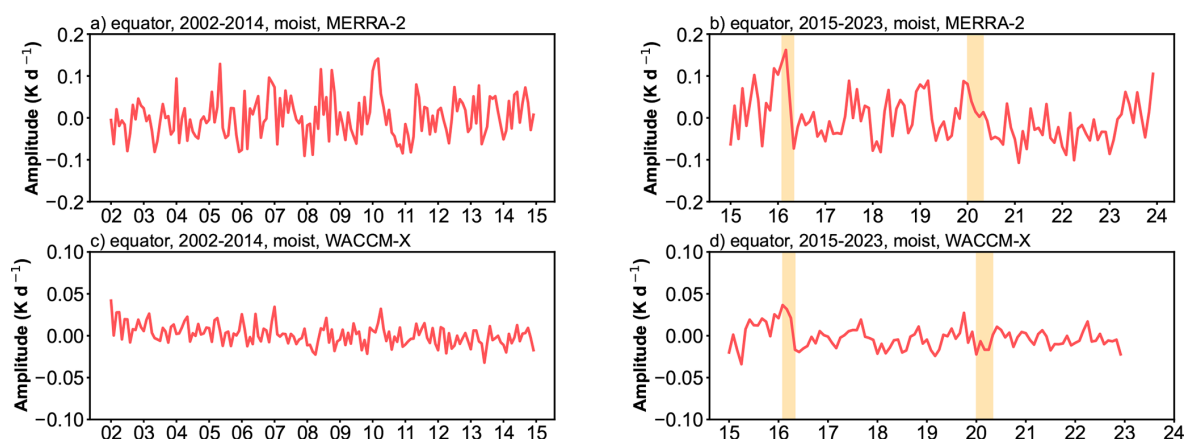


**Figure 9.** (a, b) The deseasonalized time series of DW1 amplitudes of latent heating rate ( $\text{K d}^{-1}$ ) at equator averaged from 800 to 200 hPa derived from MERRA-2. (c–d) As in panels (a)–(b) but from SD-WACCM-X. The orange-filled areas represent two QBO disruption events.

2021). Consequently, zonal wind could also influence the dissipation process. To examine the dissipation during the event, we apply the amplitude ratio method.

As in Forbes and Vincent (1989), the amplitude growth equation is:

$$\frac{A(z)}{A(70)} = \exp \left\{ \int_{70}^z \left[ -k_i + \frac{1}{2H} \right] dz \right\} \quad (3)$$

where  $A$  is the amplitude,  $z$  is the altitude (in km),  $H$  is the local scale height and  $k_i$  is the imaginary part of the complex vertical wavenumber that governs the damping of the amplitude profile. Calculating the ratio of amplitude using Eq. (3) during two different QBO phases (e.g., 2016/QBOE) yields:

$$\frac{A_{2016}(z)}{A_{\text{QBOE}}(z)} = \exp \left\{ \int_{70}^z - (k_{i,2016}(z) - k_{i,\text{QBOE}}(z)) dz \right\} \quad (4)$$

The scale height term is removed, leaving the dissipation term. Thus, the changes in amplitude ratio may reflect tidal dissipation variations at the altitude.

Figure C3 presents the ratio results derived from SABER observations and SD-WACCM-X simulations. In the SABER data (Fig. C3a), during the 2016 event, two distinct peaks appear in the lower stratosphere near 22 and 30 km when comparing the disruption events with the QBOE phase (green lines), possibly indicating relatively less dissipation during the 2016 QBO disruptions. During the 2020 event, the lower peak ( $\sim 22$  km) is close to that during 2016 event, while the upper peak ( $\sim 30$  km) is relative weak to the 2016 event. This may suggest a relatively large dissipation at those heights. The SD-WACCM-X simulations reproduce a similar pattern, although the peak altitudes differ slightly. All simulated ratios remain above 1, which may indicate stronger tidal source activity in the SD-WACCM-X simulations. Overall, these results suggest that during QBO disruptions, zonal wind may

lead to relatively less dissipation processes, thereby affecting DW1 amplitudes.

In addition to zonal-mean wind effects, latitudinal shear of zonal wind in the subtropical mesosphere can modulate the seasonal variability of the (1, 1) mode (McLandress, 2002b; Mayr and Mengel, 2005; Sakazaki et al., 2013; Kogure and Liu, 2021; Siddiqui et al., 2022). Large values of  $|\partial u / \partial y|$  at some heights are equivalent in some sense to faster rotation, which restricts the latitudinal band or waveguide where the diurnal tide can propagate vertically, thus reducing the tidal amplitude above by removing tidal energy at that altitude (McLandress, 2002b; Siddiqui et al., 2022). The wind shear at  $18^\circ \text{N/S}$  is a typical indicator (Kogure and Liu, 2021).

The monthly  $|\partial u / \partial y|$  at  $18^\circ \text{N/S}$  is calculated, deseasonalized, and classified following the method described in Sect. 3.1. The  $|\partial u / \partial y|$  profiles for different QBO phases are shown in Fig. 10. During QBOW, a pronounced negative anomaly appears near 30 km, whereas during QBOE a strong positive anomaly is evident at the same altitude. During the 2016 disruption event, the  $|\partial u / \partial y|$  profile at  $18^\circ \text{N}$  exhibits a structure broadly similar to that of QBOW. However, from 35 to 45 km it shows strong positive values, a feature not observed in other QBO phases. The  $|\partial u / \partial y|$  profile at  $18^\circ \text{S}$  displays a similar vertical structure but with smaller amplitudes. Based on this structure, the tide may be amplified near 30 km and subsequently damped near 40 km, which could partly explain why the tidal amplitudes during the 2016 disruption do not reach those observed in QBOW. In contrast, the  $|\partial u / \partial y|$  during the 2020 disruption event closely resembles the QBOE structure, suggesting that the tidal propagation background was similar to QBOE conditions.

#### 4.3 Contribution of Tide-gravity wave interaction during the events

The mesospheric diurnal tides are also affected by the interaction with GWs (Liu and Hagan, 1998; Mayr et al., 1998;

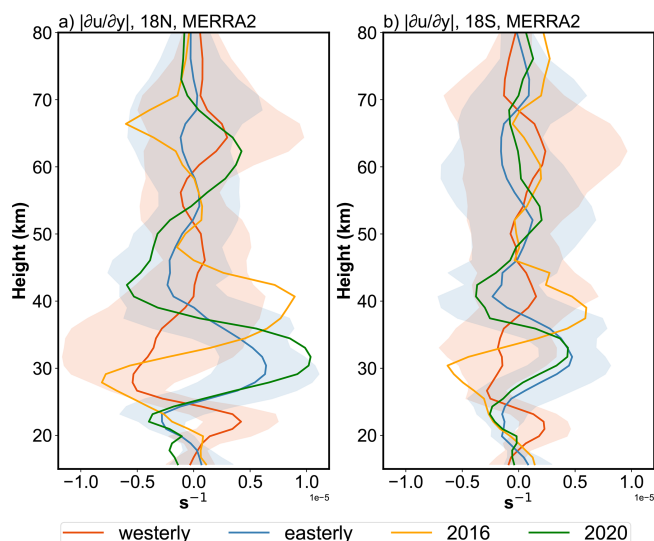


**Figure 10.** The  $|\partial u/\partial y|$  profiles after deseasonalized between different QBO phases at (a) 18° N and (b) 18° S. The colourful shaded areas denote one standard deviation of the phases for each height.

McLandress, 2002a; Li et al., 2009; Lu et al., 2012; Yang et al., 2018; Stober et al., 2021; Cen et al., 2022). These interactions can strongly modulate tidal amplitude and phase (Liu and Hagan, 1998; Lu et al., 2009; Li et al., 2009; Wang et al., 2024). In the mesosphere, gravity-wave drag may be linked to the QBO. As discussed in Wang et al. (2024), QBO-dependent zonal wind shear and associated zero-wind lines filter the upward-propagating gravity waves that can reach the mesosphere, making the gravity wave drag exhibit QBO-like features. In the tropical region of the mesosphere, due to the strong interaction between the GWs and the semi-annual oscillation (SAO) in zonal wind, the GWs in the mesosphere exhibit a weak QBO signature. QBO-related variations in GWs primarily exists in the mid-latitude mesosphere.

To quantify the GW forcing on the DW1, the methods of Yang et al. (2018) and Cen et al. (2022) are applied. The equation is:

$$GW_{\text{forcing}} = GW_{\text{drag}} \cdot \cos(\omega \cdot (\phi_{\text{GW}} - (\phi_T - 6))) \quad (5)$$

Where the  $GW_{\text{drag}}$  is the DW1 amplitude of GW drag,  $\omega$  is the  $24/2\pi$ ,  $\phi_{\text{GW}}$  is the DW1 phase of GW drag while  $\phi_T$  is DW1 amplitude of temperature.

After calculating the GW forcing, the classification method described in Sect. 3.1 is applied. As shown in Fig. D1, GW tends to damp the DW1 amplitude at nearly all latitudes above 105 km. Below  $\sim 105$  km, the GWs tend to damp the DW1 amplitude at the equator while enhancing it at subtropical latitudes. Differences exist in the amplitude of gravity wave drag between different QBO phases. Figure 11 shows the differences in GW forcing between QBO phases, with dots indicating regions exceeding the 95 % significance level. During QBOW (Fig. 11c), the equatorial

damping and subtropical enhancement are stronger than during QBOE. During the 2016 QBO disruption event, the pattern closely resembles the QBOW – QBOE difference but exhibits a larger magnitude than QBOW (Fig. 11a). During the 2020 disruption event, the GW drag is similar to QBOW conditions and is stronger than in QBOE. These results suggest that GW forcing exerts a significant influence on the modulation of DW1 amplitudes across QBO phases and disruption events.

## 5 Summary

In this work, the response of global DW1 amplitudes and phases during QBO disruption events is investigated using SABER observation, MERRA-2 dataset and SD-WACCM-X simulation results from 2002 to 2023. Additionally, the underlying mechanisms associated with these events are explored. The findings are summarized as follows:

1. There are clear differences in (1, 1) mode vertical phase structure and wavelengths between QBO westerly phases and easterly phases. The DW1 (1, 1) mode vertical phase structure and wavelengths during these two QBO disruption events are similar to those during QBO westerly phases.
2. During the 2016 QBO disruption event, DW1 amplitudes are markedly enhanced relative to regular QBOE but remain lower than those during QBOW. In the mesosphere and lower thermosphere (MLT), the amplitudes increase by  $\sim 1.56$  K ( $\sim 20.5$  %) at the equator and  $\sim 0.54$  K ( $\sim 14.4$  %) at 30° N/S yet are smaller than those during QBOW by  $\sim 1.22$  K ( $\sim 10.2$  %) at the equator. A pronounced difference of the DW1 (1, 1) mode relative to QBOW and QBOE is also evident in the stratosphere, with amplitudes  $\sim 0.21$  K ( $\sim 21$  %) higher than during QBOE and  $\sim 0.15$  K ( $\sim 10.9$  %) weaker than during QBOW.

By contrast, the 2020 disruption shows only a modest rise in DW1 amplitude relative to the regular QBOE and remain much weaker than during QBOW. In the MLT, the amplitudes rise by  $\sim 0.50$  K ( $\sim 6.0$  %) at the equator and  $\sim 0.26$  K ( $\sim 7.7$  %) at 30° N/S compared to QBOE, but are smaller than those during QBOW by 2.3 K ( $\sim 21.1$  %) and 0.57 K ( $\sim 12.0$  %), respectively. In the stratosphere, the amplitudes are about 0.18 K ( $\sim 17.0$  %) larger than during QBOE but  $\sim 0.18$  K ( $\sim 12.5$  %) lower than during QBOW.

3. During the 2016 event, the stronger water vapour radiative heating ( $\sim 8.3$  % relative to QBOE and  $\sim 10.9$  % relative to QBOW) and latent heating (22 % relative to both QBO phases) enhance the tides at their source region. The enhanced water vapour radiative heating is jointly modulated by 2016 QBO disruption and 2015/16

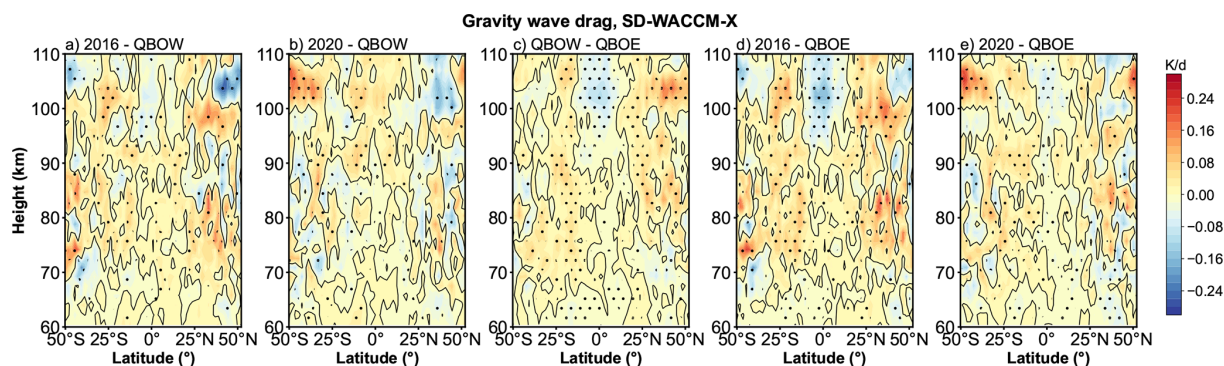


**Figure 11.** Similar to Fig. 2 but the difference of gravity wave forcing. Panels (a)–(e) give the difference result derived from SD-WACCM-X.

El Niño event, whereas the enhanced latent heating is mainly due to the 2015/16 El Niño event. Weak dissipation (zonal winds) and less tidal energy removal (zonal wind latitudinal shear) during the tide propagate upward in the lower stratosphere do not tend to suppress DW1 amplitudes, while gravity waves strengthen DW1 in the subtropics and damp it at the equator. Nevertheless, a stronger shear near  $\sim 40$  km likely prevents DW1 amplitudes from reaching the levels observed during normal QBO westerly phases. Overall, the joint modulation of water-vapor radiative heating, latent heating, weak dissipation, weak energy removal and positive GW drag contribute to a significant increase in DW1 amplitudes.

In contrast, during the 2020 event, only water vapour radiative heating exhibits a clear rise ( $\sim 5\%$ ). The dissipation and the tidal energy removal in the stratosphere become larger, effectively suppressing DW1 enhancement. The gravity-wave effect was weaker than in 2016 but still stronger than in QBOE. Consequently, the combined influence of water-vapor radiative heating and GW drag contribute to a slight increase in DW1 amplitudes relative to QBOE.

This work analyzes how the DW1 varies when the highly unusual wind of QBO occurs. This phenomenon which is found in responses at different atmospheric layers suggests an atmosphere coupling process. The observations and model simulations give clear evidence of the connection. The possible link between the lower atmosphere trace gases variation and MLT dynamic features is shown during these unique events. The result gives a window for exploring the mechanism of the coupling, providing a basis for future research on the underlying mechanisms.

## Appendix A: Approach for calculating the water vapor radiative heating rate

The heating rate for water vapor mainly follows the method from Groves (1982) and Lieberman et al. (2003). As mentioned in Eq. (1), the heating rate could be categorized into clear sky and cloudy sky. The equation of clear sky is given by Lacis and Hansen (1974):

$$J_{\text{clr}} = q\eta^c S_0 \cos \zeta \left[ MA(y) + \frac{5}{3} RA(y') \right] \quad (\text{A1})$$

with  $q$  is water vapor mixing ratio (specific humidity),  $\eta$  is defined as  $p/p_0$ ,  $c$  is defined as  $0.75 - \Gamma R_M/2g$ .  $\Gamma$  is the vertical lapse rate, which is  $6.5 \text{ K km}^{-1}$ .  $R_M$  is the gas constant for air.  $g$  is the acceleration of gravity.  $S_0$  is the solar constant, which is  $1353 \text{ W m}^{-2}$ .  $\zeta$  is the solar zenith angle, the equation is:

$$\cos \zeta = \sin \theta \sin \delta + \cos \theta \cos \delta \cos t' \quad (\text{A2})$$

with  $\theta$  is the latitude,  $\delta$  is the solar declination.  $t'$  is given by following equation:

$$t' = \lambda + \Omega t \quad (\text{A3})$$

with  $\lambda$  is longitude in radian,  $\Omega$  is the angular frequency of Earth's rotation.  $t$  is the universal time.

$M$  is given by equation:

$$M = \frac{35}{(1224 \cos^2 \zeta + 1)^{\frac{1}{2}}} \quad (\text{A4})$$

$A(y)$  is given by equation:

$$A(y) = 2.9 \left[ \frac{0.635 + 0.365Y}{(Y^{0.635} + 5.925y)^2 Y^{0.365}} \right] \text{ cm}^2 \text{ g}^{-1} \quad (\text{A5})$$

with:

$$Y = 1 + 141.5y \quad (\text{A6})$$

and

$$y = M\bar{w} \quad (\text{A7})$$

and

$$y' = M\bar{w}_t + \frac{5}{3}(\bar{w}_t - \bar{w}) \quad (\text{A8})$$

The  $\bar{w}$  is the effective water vapor amount, is given by equation:

$$\bar{w} = \int_z^\infty q\rho(p/p_0)^{0.75}(T_0/T)^{1/2}dz \quad (\text{A9})$$

Where  $\rho$  is the air density.  $\bar{w}_t$  is the total water vapor above the reflecting surface.

The cloudy sky heating rate is given by Groves (1982):

$$J_{\text{cld}} = q\eta^c S_0 \cos \zeta Z \quad (\text{A10})$$

with  $Z$  is parameter given by:

$$Z = \sum_i \{ak' [\cosh(\xi_0 + \beta - \xi) - \cosh(\xi_0 + \beta' - \xi)] / \sinh(\xi_0 + \beta)\}_i \quad (\text{A11})$$

with  $\xi$  is given by:

$$\xi = k'\bar{w} \quad (\text{A12})$$

$$k' = \frac{5}{3}\alpha(\sigma + k) \quad (\text{A13})$$

with  $\alpha$ ,  $\beta$  and  $\beta'$ :

$$\alpha = (1 - \omega)^{\frac{1}{2}}(1 + \omega - 2\omega f)^{\frac{1}{2}} \quad (\text{A14})$$

$$\beta = \frac{1}{2} \ln \left\{ [1 + \alpha - \omega f - R\omega(1 - f)] \div [1 - \alpha - \omega f - R\omega(1 - f)] \right\} \quad (\text{A15})$$

$$\beta' = \beta + \frac{1}{2} \ln \left[ \frac{1 - \alpha - \omega f}{1 + \alpha - \omega f} \right] \quad (\text{A16})$$

with single scattering albedo:

$$\omega = \frac{\sigma}{\sigma + k} \quad (\text{A17})$$

where  $\sigma = 40 \text{ cm}^{-1}$ ,  $f$  is 0.925,  $k$  and  $a$  are given by table 2 from Somerville et al. (1974).

## Appendix B: Approach for calculating the ozone radiative heating rate

The heating rate for ozone mainly uses the equations from Strobel/Zhu model (Strobel, 1978; Zhu, 1994) and processing method from Xu et al. (2010). The Chappius, Hartley and

Huggins bands are as follow:

$$\frac{H_{\text{Ch}}}{[\text{O}_3]} = F_{\text{C}}\sigma_{\text{C}}\exp[-\sigma_{\text{C}}N_3] \quad (\text{B1})$$

$$\frac{H_{\text{Ha}}}{[\text{O}_3]} = F_{\text{Ha}}\sigma_{\text{Ha}}\exp[-\sigma_{\text{Ha}}N_3] \quad (\text{B2})$$

$$\frac{H_{\text{Hu}}}{[\text{O}_3]} = \frac{1}{MN_3} \left\{ I_1 + (I_2 - I_1)\exp[-\sigma_{\text{Hu}}N_3e^{-M\lambda_{\text{long}}}] - I_2\exp[-\sigma_{\text{Hu}}N_3e^{-M\lambda_{\text{short}}}] \right\} \quad (\text{B3})$$

The  $[\text{O}_3]$  is the ozone number density while the  $N_3$  is the column density of  $\text{O}_3$  along the solar radiation path. For Eq. (B1), the  $F_{\text{C}}$  is  $370 \text{ J m}^{-2} \text{ s}^{-1}$ , the  $\sigma_{\text{C}}$  is  $2.85 \times 10^{-25}$ . For Eq. (B2), the  $F_{\text{Ha}}$  is  $5.13 \text{ J m}^{-2} \text{ s}^{-1}$ , the  $\sigma_{\text{Ha}}$  is  $8.7 \times 10^{-22} \text{ m}^{-2}$ . For Eq. (B3), the  $I_1$  is  $0.07 \text{ J m}^{-2} \text{ s}^{-1} \text{ \AA}^{-1}$ , the  $I_2$  is  $0.07 \text{ J m}^{-2} \text{ s}^{-1} \text{ \AA}^{-1}$ ,  $M$  is  $0.01273 \text{ \AA}^{-1}$ ,  $\lambda_{\text{long}}$  is  $2805 \text{ \AA}^{-1}$ ,  $\lambda_{\text{short}}$  is  $3015 \text{ \AA}^{-1}$ ,  $\sigma_{\text{Hu}}$  is  $1.15 \times 10^{-6} \text{ m}^{-2}$ .

For the heating rate calculation, the ozone density profiles are firstly interpolated to a uniform vertical grid with 1 km spacing from 20 to 105 km. Then the ozone profiles are processing into zonal mean overlapping latitude bins that are 10 degrees wide with centres offset by  $5^\circ$  from  $50^\circ \text{ S}$ – $50^\circ \text{ N}$ . The diurnal variation of the vertical profile of the ozone heating rate in each latitude bin is calculated using the SABER ozone density and Eqs. (B1)–(B3), along with the diurnal variation of solar zenith angle for the specific latitude and day of year.

## Appendix C: The feature of DW1 (1, 1) Hough mode

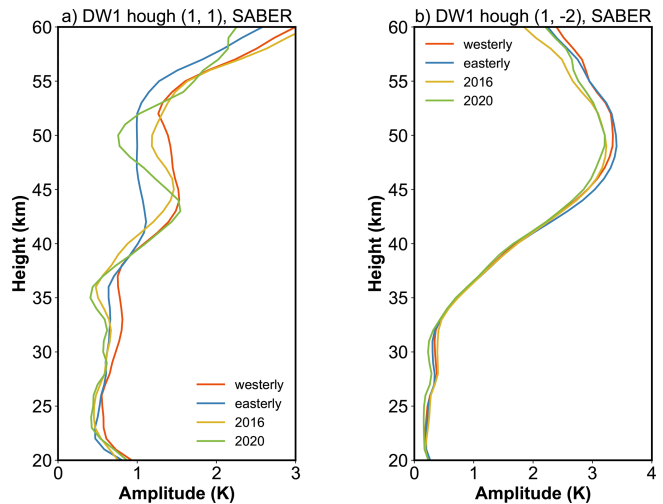


**Figure C1.** Amplitude profiles of DW1 (a) (1,1) and (b) (1, -2) modes during different QBO phases.



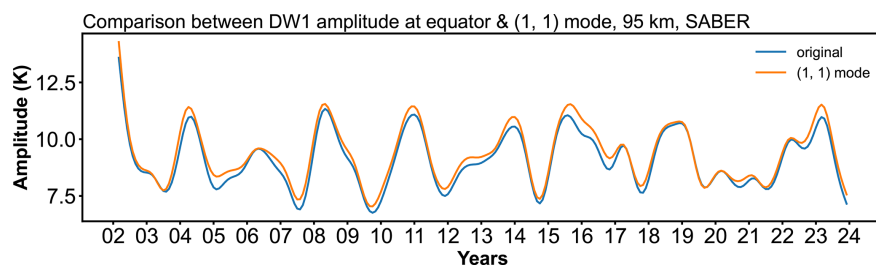


**Figure C2.** The amplitude time series of equatorial DW1 and (1, 1) Hough mode at 95 km.

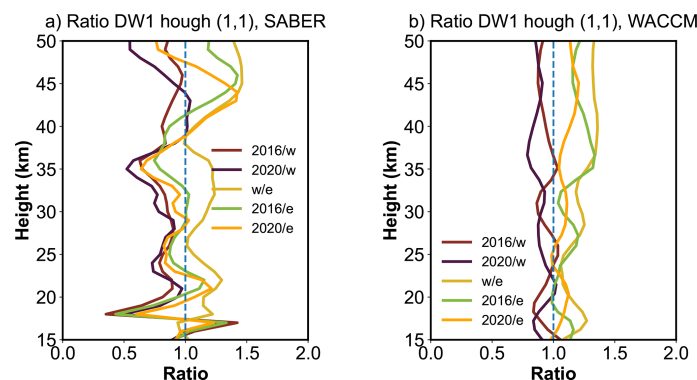


**Figure C3.** the vertical profile of DW1 (1, 1) mode amplitude ratio derived from 2016/westerly (dark red), 2020/westerly (dark purple), westerly/easterly (yellow), 2016/easterly (green), and 2020/easterly (orange). The dashed blue lines represent the ratio of 1.

#### Appendix D: Gravity wave drag effect to DW1

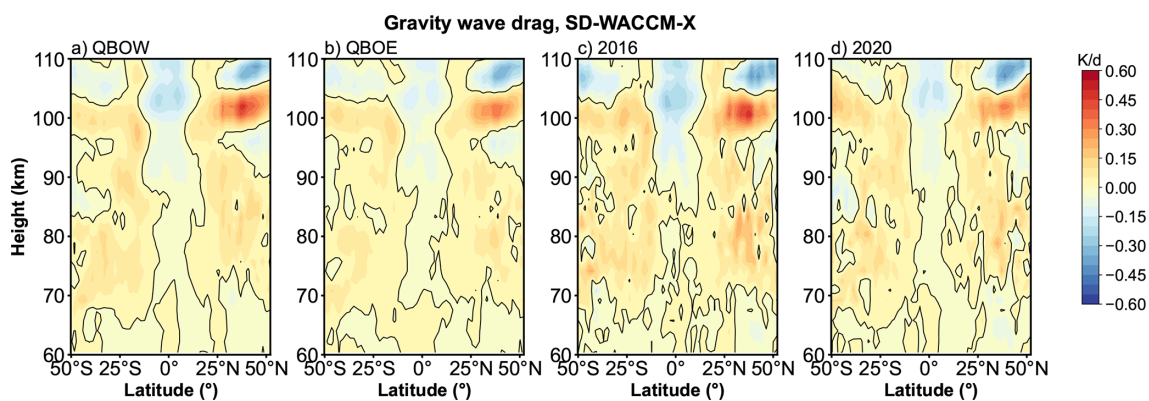


**Figure D1.** The gravity wave forcing on DW1 during difference QBO phases as a function of latitude and altitude.

**Data availability.** SABER data is available from the SABER project data server at <https://spdf.gsfc.nasa.gov/pub/data/timed/saber/> (last access: 20 May 2025). The SD-WACCM-X is retrieved from [https://app.globus.org/file-manager?origin\\_id=d2762023-6ab4-46c9-ab12-b037cd568e42&origin\\_path=%2F](https://app.globus.org/file-manager?origin_id=d2762023-6ab4-46c9-ab12-b037cd568e42&origin_path=%2F) (last access: 20 May 2025) (login required). The QBO index is retrieved from [https://acd-ext.gsfc.nasa.gov/Data\\_services/met/qbo/QBO\\_Singapore\\_Uvals\\_GSFC.txt](https://acd-ext.gsfc.nasa.gov/Data_services/met/qbo/QBO_Singapore_Uvals_GSFC.txt) (last access: 20 May 2025). The Generalized Lomb-Scargle Periodogram and best-frequency fit method are provided by PyAstronomy (<https://github.com/sczesla/PyAstronomy>, last access: 20 May 2025) (Czesla et al., 2019). The MERRA-2 reanalysis data can be retrieved from <https://doi.org/10.5067/WWQSQ8IVFW8> (GMAO, 2015a; zonal wind, temperature, cloud fraction, specific humidity), <https://doi.org/10.5067/LTVB4GPCOTK2> (GMAO, 2015b; air density), <https://doi.org/10.5067/Q9QMY5PBNV1T> (GMAO, 2015c; surface albedo), <https://doi.org/10.5067/9NCR9DDDOPFI> (GMAO, 2015d; tendency of air temperature due to moist processes).

**Author contributions.** Conceptualization: SL, GYJ; investigation: SL; methodology: SL, GYJ; project administration: BXL, GYJ and YJZ; software: SL; supervision: GYJ, BXL and YJZ; validation: BXL, GYJ and YJZ; visualization: SL; writing – original draft preparation: SL; and writing – review and editing: GYJ, BXL, XL, JYX, YJZ and WY. All authors have read and agreed to the published version of the paper.

**Competing interests.** The contact author has declared that none of the authors has any competing interests.

**Disclaimer.** Publisher's note: Copernicus Publications remains neutral with regard to jurisdictional claims made in the text, published maps, institutional affiliations, or any other geographical representation in this paper. While Copernicus Publications makes every effort to include appropriate place names, the final responsibility lies with the authors. Views expressed in the text are those of the authors and do not necessarily reflect the views of the publisher.

**Acknowledgements.** WACCM-X SD output data have been used in this study, and we would like to acknowledge the WACCM-X development group at NCAR/HAO for making the model output publicly available. This work was jointly supported by the Strategic Priority Research Program of the Chinese Academy of Sciences (Grant No. XDB0560000), the Pandeng Program of National Space Science Center CAS, National Key R&D program of China (2023YFB3905100), the Project of Stable Support for Youth Team in Basic Research Field, CAS (YSBR-018), the National Natural Science Foundation of China (42174212), the Chinese Meridian Project, and the Specialized Research Fund for State Key Laboratories.

**Financial support.** This work was jointly supported by the Strategic Priority Research Program of the Chinese Academy of

Sciences (grant no. XDB0560000), the Pandeng Program of National Space Science Center CAS, National Key R&D program of China (grant no. 2023YFB3905100), the Project of Stable Support for Youth Team in Basic Research Field, CAS (grant no. YSBR-018), the National Natural Science Foundation of China (grant no. 42174212), the Chinese Meridian Project, and the Specialized Research Fund for State Key Laboratories.

**Review statement.** This paper was edited by John Plane and reviewed by two anonymous referees.

## References

- Anstey, J. A., Banyard, T. P., Butchart, N., Coy, L., Newman, P. A., Osprey, S., and Wright, C. J.: Prospect of Increased Disruption to the QBO in a Changing Climate, *Geophys. Res. Lett.*, 48, <https://doi.org/10.1029/2021gl093058>, 2021.
- Araújo, L. R., Lima, L. M., Jacobi, C., and Batista, P. P.: Quasi-biennial oscillation signatures in the diurnal tidal winds over Cachoeira Paulista, Brazil, *J. Atmos. Sol. Terr. Phys.*, 155, 71–78, <https://doi.org/10.1016/j.jastp.2017.02.001>, 2017.
- Baldwin, M. P., Gray, L. J., Dunkerton, T. J., Hamilton, K., Haynes, P. H., Randel, W. J., Holton, J. R., Alexander, M. J., Hirota, I., Horinouchi, T., Jones, D. B. A., Kinnersley, J. S., Marquardt, C., Sato, K., and Takahashi, M.: The quasi-biennial oscillation, *Rev. Geophys.*, 39, 179–229, <https://doi.org/10.1029/1999rg000073>, 2001.
- Barton, C. A. and McCormack, J. P.: Origin of the 2016 QBO Disruption and Its Relationship to Extreme El Niño Events, *Geophys. Res. Lett.*, 44, <https://doi.org/10.1002/2017gl075576>, 2017.
- Cen, Y., Yang, C., Li, T., Russell III, J. M., and Dou, X.: Suppressed migrating diurnal tides in the mesosphere and lower thermosphere region during El Niño in northern winter and its possible mechanism, *Atmos. Chem. Phys.*, 22, 7861–7874, <https://doi.org/10.5194/acp-22-7861-2022>, 2022.
- Chapman, S. and Lindzen, R.: *Atmospheric tides – thermal and gravitational*, D. Reidel Publishing Company, Dordrecht, the Netherlands, ISBN 978-94-010-3401-2, 1970.
- Coy, L., Newman, P. A., Pawson, S., and Lait, L. R.: Dynamics of the Disrupted 2015/16 Quasi-Biennial Oscillation, *J. Clim.*, 30, 5661–5674, <https://doi.org/10.1175/jcli-d-16-0663.1>, 2017.
- Czesla, S., Schröter, S., Schneider, C. P., Huber, K. F., Pfeifer, F., Andreasen, D. T., and Zechmeister, M.: PyA: Python astronomy-related packages, GitHub [code], <https://github.com/sczesla/PyAstronomy> (last access: 20 May 2025), 2019.
- Davis, R. N., Du, J., Smith, A. K., Ward, W. E., and Mitchell, N. J.: The diurnal and semidiurnal tides over Ascension Island (°S, 14°W) and their interaction with the stratospheric quasi-biennial oscillation: studies with meteor radar, eCMAM and WACCM, *Atmos. Chem. Phys.*, 13, 9543–9564, <https://doi.org/10.5194/acp-13-9543-2013>, 2013.
- Dhadly, M. S., Emmert, J. T., Drob, D. P., McCormack, J. P., and Niciejewski, R. J.: Short-Term and Interannual Variations of Migrating Diurnal and Semidiurnal Tides in the Mesosphere and Lower Thermosphere, *J. Geophys. Res.: Space Phys.*, 123, 7106–7123, <https://doi.org/10.1029/2018ja025748>, 2018.

- Diallo, M., Riese, M., Birner, T., Konopka, P., Müller, R., Hegglin, M. I., Santee, M. L., Baldwin, M., Legras, B., and Ploeger, F.: Response of stratospheric water vapor and ozone to the unusual timing of El Niño and the QBO disruption in 2015–2016, *Atmos. Chem. Phys.*, 18, 13055–13073, <https://doi.org/10.5194/acp-18-13055-2018>, 2018.
- Diallo, M. A., Ploeger, F., Hegglin, M. I., Ern, M., Groöf, J.-U., Khaykin, S., and Riese, M.: Stratospheric water vapour and ozone response to the quasi-biennial oscillation disruptions in 2016 and 2020, *Atmos. Chem. Phys.*, 22, 14303–14321, <https://doi.org/10.5194/acp-22-14303-2022>, 2022.
- Ern, M., Ploeger, F., Preusse, P., Gille, J. C., Gray, L. J., Kalisch, S., Mlynarczyk, M. G., Russell, J. M., and Riese, M.: Interaction of gravity waves with the QBO: A satellite perspective, *J. Geophys. Res.: Atmos.*, 119, 2329–2355, <https://doi.org/10.1002/2013jd020731>, 2014.
- Forbes, J. M. and Garrett, H. B.: Seasonal-Latitudinal Structure of the Diurnal Thermospheric Tide, *J. Atmos. Sci.*, 35, 148–159, [https://doi.org/10.1175/1520-0469\(1978\)035<0148:Slstotd>2.0.Co;2](https://doi.org/10.1175/1520-0469(1978)035<0148:Slstotd>2.0.Co;2), 1978.
- Forbes, J. M. and Vincent, R. A.: Effects of mean winds and dissipation on the diurnal propagating tide: An analytic approach, *Planet. Space Sci.*, 37, 197–209, [https://doi.org/10.1016/0032-0633\(89\)90007-x](https://doi.org/10.1016/0032-0633(89)90007-x), 1989.
- Gan, Q., Du, J., Ward, W. E., Beagley, S. R., Fomichev, V. I., and Zhang, S.: Climatology of the diurnal tides from eCMAM30 (1979 to 2010) and its comparison with SABER, *Earth Planets Space*, 66, <https://doi.org/10.1186/1880-5981-66-103>, 2014.
- Garcia, R. R.: On the Structure and Variability of the Migrating Diurnal Temperature Tide Observed by SABER, *J. Atmos. Sci.*, 80, 687–704, <https://doi.org/10.1175/jas-d-22-0167.1>, 2023.
- Garcia, R. R., Marsh, D. R., Kinnison, D. E., Boville, B. A., and Sassi, F.: Simulation of secular trends in the middle atmosphere, 1950–2003, *J. Geophys. Res.: Atmos.*, 112, <https://doi.org/10.1029/2006jd007485>, 2007.
- Gelaro, R., McCarty, W., Suarez, M. J., Todling, R., Molod, A., Takacs, L., Randles, C., Darmenov, A., Bosilovich, M. G., Reichle, R., Wargan, K., Coy, L., Cullather, R., Draper, C., Akella, S., Buchard, V., Conaty, A., da Silva, A., Gu, W., Kim, G. K., Koster, R., Lucchesi, R., Merkova, D., Nielsen, J. E., Partyka, G., Pawson, S., Putman, W., Rienecker, M., Schubert, S. D., Sienkiewicz, M., and Zhao, B.: The Modern-Era Retrospective Analysis for Research and Applications, Version 2 (MERRA-2), *J. Clim.*, 30, 5419–5454, <https://doi.org/10.1175/JCLI-D-16-0758.1>, 2017.
- Global Modeling and Assimilation Office (GMAO): MERRA-2 inst3\_3d\_asm\_Nv: 3d, 3-Hourly, Instantaneous, Model-Level, Assimilation, Assimilated Meteorological Fields V5.12.4, Goddard Earth Sciences Data and Information Services Center (GES DISC), Greenbelt, MD, USA [data set], <https://doi.org/10.5067/WWQSQX8IVFW8>, 2015a.
- Global Modeling and Assimilation Office (GMAO): MERRA-2 inst3\_3d\_aer\_Nv: 3d, 3-Hourly, Instantaneous, Model-Level, Assimilation, Aerosol Mixing Ratio V5.12.4, Goddard Earth Sciences Data and Information Services Center (GES DISC), Greenbelt, MD, USA [data set], <https://doi.org/10.5067/LTVB4GPCOTK2>, 2015b.
- Global Modeling and Assimilation Office (GMAO): MERRA-2 tavg1\_2d\_rad\_Nx: 2d, 1-Hourly, Time-Averaged, Single-Level, Assimilation, Radiation Diagnostics V5.12.4, Goddard Earth Sciences Data and Information Services Center (GES DISC), Greenbelt, MD, USA [data set], <https://doi.org/10.5067/Q9QMY5PBNVIT>, 2015c.
- Global Modeling and Assimilation Office (GMAO): MERRA-2 tavg3\_3d\_tdt\_Np: 3d, 3-Hourly, Time-Averaged, Pressure-Level, Assimilation, Temperature Tendencies V5.12.4, Goddard Earth Sciences Data and Information Services Center (GES DISC), Greenbelt, MD, USA [data set], <https://doi.org/10.5067/9NCR9DDDOPFI>, 2015d.
- Groves, G. V.: Hough components of water vapour heating, *J. Atmos. Terr. Phys.*, 44, 281–290, [https://doi.org/10.1016/0021-9169\(82\)90033-2](https://doi.org/10.1016/0021-9169(82)90033-2), 1982.
- Hagan, M. E.: Comparative effects of migrating solar sources on tidal signatures in the middle and upper atmosphere, *J. Geophys. Res.: Atmos.*, 101, 21213–21222, <https://doi.org/10.1029/96jd01374>, 1996.
- Hagan, M. E., Burrage, M. D., Forbes, J. M., Hackney, J., Randel, W. J., and Zhang, X.: QBO effects on the diurnal tide in the upper atmosphere, *Earth Planets Space*, 51, 571–578, <https://doi.org/10.1186/BF03353216>, 1999.
- Holton, J. R. and Lindzen, R. S.: An Updated Theory for the Quasi-Biennial Cycle of the Tropical Stratosphere, *J. Atmos. Sci.*, 29, 1076–1080, [https://doi.org/10.1175/1520-0469\(1972\)029<1076:Autftq>2.0.Co;2](https://doi.org/10.1175/1520-0469(1972)029<1076:Autftq>2.0.Co;2), 1972.
- Hu, S. and Fedorov, A. V.: The extreme El Niño of 2015–2016 and the end of global warming hiatus, *Geophys. Res. Lett.*, 44, 3816–3824, <https://doi.org/10.1002/2017gl072908>, 2017.
- Jiang, G., Xu, J., Shi, J., Yang, G., Wang, X., and Yan, C.: The first observation of the atmospheric tides in the mesosphere and lower thermosphere over Hainan, China, *Chin. Sci. Bull.*, 55, 1059–1066, <https://doi.org/10.1007/s11434-010-0084-8>, 2010.
- Johnston, B. R., Randel, W. J., and Braun, J. J.: Interannual Variability of Tropospheric Moisture and Temperature and Relationships to ENSO Using COSMIC-1 GNSS-RO Retrievals, *J. Clim.*, 35, 7109–7125, <https://doi.org/10.1175/jcli-d-21-0884.1>, 2022.
- Kang, M.-J. and Chun, H.-Y.: Contributions of equatorial waves and small-scale convective gravity waves to the 2019/20 quasi-biennial oscillation (QBO) disruption, *Atmos. Chem. Phys.*, 21, 9839–9857, <https://doi.org/10.5194/acp-21-9839-2021>, 2021.
- Kang, M.-J., Chun, H.-Y., Son, S.-W., Garcia, R. R., An, S.-I., and Park, S.-H.: Role of tropical lower stratosphere winds in quasi-biennial oscillation disruptions, *Sci. Adv.*, 8, <https://doi.org/10.1126/sciadv.abm7229>, 2022.
- Kogure, M. and Liu, H.: DW1 Tidal Enhancements in the Equatorial MLT During 2015 El Niño: The Relative Role of Tidal Heating and Propagation, *J. Geophys. Res.: Space Phys.*, 126, <https://doi.org/10.1029/2021ja029342>, 2021.
- Kogure, M., Liu, H., and Jin, H.: Impact of Tropospheric Ozone Modulation Due To El Niño on Tides in the MLT, *Geophys. Res. Lett.*, 50, <https://doi.org/10.1029/2023gl102790>, 2023.
- Lacis, A. A. and Hansen, J.: A Parameterization for the Absorption of Solar Radiation in the Earth's Atmosphere, *J. Atmos. Sci.*, 31, 118–133, [https://doi.org/10.1175/1520-0469\(1974\)031<0118:Apftao>2.0.Co;2](https://doi.org/10.1175/1520-0469(1974)031<0118:Apftao>2.0.Co;2), 1974.
- Li, T., She, C. Y., Liu, H. L., Yue, J., Nakamura, T., Krueger, D. A., Wu, Q., Dou, X., and Wang, S.: Observation of local tidal variability and instability, along with dissipation of diurnal tidal harmonics in the mesopause region over Fort Collins,

- Colorado (41° N, 105° W), *J. Geophys. Res.: Atmos.*, 114, <https://doi.org/10.1029/2008jd011089>, 2009.
- Lieberman, R. S., Ortland, D. A., and Yarosh, E. S.: Climatology and interannual variability of diurnal water vapor heating, *J. Geophys. Res.: Atmos.*, 108, <https://doi.org/10.1029/2002jd002308>, 2003.
- Lieberman, R. S., Riggins, D. M., Ortland, D. A., Nesbitt, S. W., and Vincent, R. A.: Variability of mesospheric diurnal tides and tropospheric diurnal heating during 1997–1998, *J. Geophys. Res.*, 112, <https://doi.org/10.1029/2007jd008578>, 2007.
- Lindzen, R. S. and Holton, J. R.: A Theory of the Quasi-Biennial Oscillation, *J. Atmos. Sci.*, 25, 1095–1107, [https://doi.org/10.1175/1520-0469\(1968\)025<1095:Atotqb>2.0.Co;2](https://doi.org/10.1175/1520-0469(1968)025<1095:Atotqb>2.0.Co;2), 1968.
- Liu, G., Lieberman, R. S., Harvey, V. L., Pedatella, N. M., Oberheide, J., Hibbins, R. E., Espy, P. J., and Janches, D.: Tidal Variations in the Mesosphere and Lower Thermosphere Before, During, and After the 2009 Sudden Stratospheric Warming, *J. Geophys. Res.: Space Phys.*, 126, <https://doi.org/10.1029/2020ja028827>, 2021.
- Liu, H. L. and Hagan, M. E.: Local heating/cooling of the mesosphere due to gravity wave and tidal coupling, *Geophys. Res. Lett.*, 25, 2941–2944, <https://doi.org/10.1029/98gl02153>, 1998.
- Liu, H. L., Foster, B. T., Hagan, M. E., McInerney, J. M., Maute, A., Qian, L., Richmond, A. D., Roble, R. G., Solomon, S. C., Garcia, R. R., Kinnison, D., Marsh, D. R., Smith, A. K., Richter, J., Sassi, F., and Oberheide, J.: Thermosphere extension of the Whole Atmosphere Community Climate Model, *J. Geophys. Res.: Space Phys.*, 115, <https://doi.org/10.1029/2010ja015586>, 2010.
- Liu, H. L., Bardeen, C. G., Foster, B. T., Lauritzen, P., Liu, J., Lu, G., Marsh, D. R., Maute, A., McInerney, J. M., Pedatella, N. M., Qian, L., Richmond, A. D., Roble, R. G., Solomon, S. C., Vitt, F. M., and Wang, W.: Development and Validation of the Whole Atmosphere Community Climate Model With Thermosphere and Ionosphere Extension (WACCM – X 2.0), *J. Adv. Model. Earth Syst.*, 10, 381–402, <https://doi.org/10.1002/2017ms001232>, 2018.
- Liu, M., Xu, J., Liu, H., and Liu, X.: Possible modulation of migrating diurnal tide by latitudinal gradient of zonal wind observed by SABER/TIMED, *Science China Earth Sciences*, 59, 408–417, <https://doi.org/10.1007/s11430-015-5185-4>, 2015.
- Liu, S., Jiang, G., Luo, B., Xu, J., Lin, R., Zhu, Y., and Liu, W.: Solar Cycle Dependence of Migrating Diurnal Tide in the Equatorial Mesosphere and Lower Thermosphere, *Remote Sens.*, 16, <https://doi.org/10.3390/rs16183437>, 2024a.
- Liu, Y., Xu, J., Smith, A. K., and Liu, X.: Seasonal and Interannual Variations of Global Tides in the Mesosphere and Lower Thermosphere Neutral Winds: I. Diurnal Tides, *J. Geophys. Res.: Space Phys.*, 129, <https://doi.org/10.1029/2023ja031887>, 2024b.
- Lu, X., Liu, A. Z., Swenson, G. R., Li, T., Leblanc, T., and McDermid, I. S.: Gravity wave propagation and dissipation from the stratosphere to the lower thermosphere, *J. Geophys. Res.: Atmos.*, 114, <https://doi.org/10.1029/2008jd010112>, 2009.
- Lu, X., Liu, H. L., Liu, A. Z., Yue, J., McInerney, J. M., and Li, Z.: Momentum budget of the migrating diurnal tide in the Whole Atmosphere Community Climate Model at vernal equinox, *J. Geophys. Res.: Atmos.*, 117, <https://doi.org/10.1029/2011jd017089>, 2012.
- Marsh, D. R., Mills, M. J., Kinnison, D. E., Lamarque, J.-F., Calvo, N., and Polvani, L. M.: Climate Change from 1850 to 2005 Simulated in CESM1(WACCM), *J. Clim.*, 26, 7372–7391, <https://doi.org/10.1175/jcli-d-12-00558.1>, 2013.
- Mayr, H. G., Mengel, J. G., Chan, K. L., and Porter, H. S.: Seasonal variations of the diurnal tide induced by gravity wave filtering, *Geophys. Res. Lett.*, 25, 943–946, <https://doi.org/10.1029/98gl00637>, 1998.
- Mayr, H. G. and Mengel, J. G.: Interannual variations of the diurnal tide in the mesosphere generated by the quasi-biennial oscillation, *J. Geophys. Res.*, 110, D10111, <https://doi.org/10.1029/2004JD005055>, 2005.
- McLandress, C.: The Seasonal Variation of the Propagating Diurnal Tide in the Mesosphere and Lower Thermosphere. Part I: The Role of Gravity Waves and Planetary Waves, *J. Atmos. Sci.*, 59, 893–906, [https://doi.org/10.1175/1520-0469\(2002\)059<0893:Tsvotp>2.0.Co;2](https://doi.org/10.1175/1520-0469(2002)059<0893:Tsvotp>2.0.Co;2), 2002a.
- McLandress, C.: The Seasonal Variation of the Propagating Diurnal Tide in the Mesosphere and Lower Thermosphere. Part II: The Role of Tidal Heating and Zonal Mean Winds, *J. Atmos. Sci.*, 59, 907–922, [https://doi.org/10.1175/1520-0469\(2002\)059<0907:Tsvotp>2.0.Co;2](https://doi.org/10.1175/1520-0469(2002)059<0907:Tsvotp>2.0.Co;2), 2002b.
- Mertens, C. J., Schmidlin, F. J., Goldberg, R. A., Remsberg, E. E., Pesnell, W. D., Russell, J. I. I., Mlynczak, M. G., Lopez-Puertas, M., Wintersteiner, P. P., Picard, R. H., Winick, J. R., and Gordley, L. L.: SABER observations of mesospheric temperatures and comparisons with falling sphere measurements taken during the 2002 summer MaCWAVE campaign, *Geophys. Res. Lett.*, 31, <https://doi.org/10.1029/2003gl018605>, 2004.
- Mertens, C. J., Mlynczak, M. G., López-Puertas, M., Wintersteiner, P. P., Picard, R. H., Winick, J. R., Gordley, L. L., and Russell, J. M.: Retrieval of mesospheric and lower thermospheric kinetic temperature from measurements of CO<sub>2</sub> 15  $\mu$ m Earth Limb Emission under non-LTE conditions, *Geophys. Res. Lett.*, 28, 1391–1394, <https://doi.org/10.1029/2000gl012189>, 2001.
- Mlynczak, M. G., Hunt, L. A., Garcia, R. R., Harvey, V. L., Marshall, B. T., Yue, J., Mertens, C. J., and Russell III, J. M.: Cooling and Contraction of the Mesosphere and Lower Thermosphere From 2002 to 2021, *J. Geophys. Res. Atmos.*, 127, <https://doi.org/10.1029/2022JD036767>, 2022.
- Mlynczak, M. G., Marshall, B. T., Garcia, R. R., Hunt, L., Yue, J., Harvey, V. L., Lopez-Puertas, M., Mertens, C., and Russell, J.: Algorithm Stability and the Long-Term Geospace Data Record From TIMED/SABER, *Geophys. Res. Lett.*, 50, <https://doi.org/10.1029/2022gl102398>, 2023.
- Mukhtarov, P., Pancheva, D., and Andonov, B.: Global structure and seasonal and interannual variability of the migrating diurnal tide seen in the SABER/TIMED temperatures between 20 and 120 km, *J. Geophys. Res.: Space Phys.*, 114, <https://doi.org/10.1029/2008ja013759>, 2009.
- Neale, R., Richter, J. H., Conley, A. J., Park, S., Lauritzen, P. H., Gettelman, A., Williamson, D., Rasch, P. J., Vavrus, S. J., Taylor, M. A., Collins, W., Zhang, M., and Lin, S.: Description of the NCAR Community Atmosphere Model (CAM 4.0), <https://doi.org/10.5065/GSEB-6470>, 2010.
- Newman, P. A., Coy, L., Pawson, S., and Lait, L. R.: The anomalous change in the QBO in 2015–2016, *Geophys. Res. Lett.*, 43, 8791–8797, <https://doi.org/10.1002/2016gl070373>, 2016.



- Oberheide, J., Forbes, J. M., Häusler, K., Wu, Q., and Bruinsma, S. L.: Tropospheric tides from 80 to 400 km: Propagation, interannual variability, and solar cycle effects, *J. Geophys. Res.: Atmos.*, 114, <https://doi.org/10.1029/2009jd012388>, 2009.
- Ortland, D. A.: Daily estimates of the migrating tide and zonal mean temperature in the mesosphere and lower thermosphere derived from SABER data, *J. Geophys. Res.: Atmos.*, 122, 3754–3785, <https://doi.org/10.1002/2016jd025573>, 2017.
- Osprey, S. M., Butchart, N., Knight, J. R., Scaife, A. A., Hamilton, K., Anstey, J. A., Schenzinger, V., and Zhang, C.: An unexpected disruption of the atmospheric quasi-biennial oscillation, *Science*, 353, 1424–1427, <https://doi.org/10.1126/science.aah4156>, 2016.
- Pedatella, N.: Ionospheric Variability during the 2020–2021 SSW: COSMIC-2 Observations and WACCM-X Simulations, *Atmosphere*, 13, <https://doi.org/10.3390/atmos13030368>, 2022.
- Pramitha, M., Kishore Kumar, K., Venkat Ratnam, M., Praveen, M., and Rao, S. V. B.: Disrupted Stratospheric QBO Signatures in the Diurnal Tides Over the Low-Latitude MLT Region, *Geophys. Res. Lett.*, 48, <https://doi.org/10.1029/2021gl093022>, 2021a.
- Pramitha, M., Kumar, K. K., Ratnam, M. V., Praveen, M., and Bhaskara Rao, S. V.: Stratospheric Quasi Biennial Oscillation Modulations of Migrating Diurnal Tide in the Mesosphere and Lower Thermosphere Over the Low and Equatorial Latitudes, *J. Geophys. Res.: Space Phys.*, 126, <https://doi.org/10.1029/2020ja028970>, 2021b.
- Qian, L., Burns, A. G., Emery, B. A., Foster, B., Lu, G., Maute, A., Richmond, A. D., Roble, R. G., Solomon, S. C., and Wang, W.: The NCAR TIE-GCM: A community model of the coupled thermosphere/ionosphere system, in: *Modeling the Ionosphere–Thermosphere System*, edited by: Joseph Huba, J., Schunk, R., and Khazanov, G., AGU Geophysical Monographs, American Geophysical Union, <https://doi.org/10.1002/9781118704417>, 2014.
- Riggin, D. M. and Lieberman, R. S.: Variability of the diurnal tide in the equatorial MLT, *J. Atmos. Sol. Terr. Phys.*, 102, 198–206, <https://doi.org/10.1016/j.jastp.2013.05.011>, 2013.
- Sakazaki, T., Fujiwara, M., and Zhang, X.: Interpretation of the vertical structure and seasonal variation of the diurnal migrating tide from the troposphere to the lower mesosphere, *J. Atmos. Sol. Terr. Phys.*, 105–106, 66–80, <https://doi.org/10.1016/j.jastp.2013.07.010>, 2013.
- Sakazaki, T., Fujiwara, M., and Shiotani, M.: Representation of solar tides in the stratosphere and lower mesosphere in state-of-the-art reanalyses and in satellite observations, *Atmos. Chem. Phys.*, 18, 1437–1456, <https://doi.org/10.5194/acp-18-1437-2018>, 2018.
- Santoso, A., McPhaden, M. J., and Cai, W.: The Defining Characteristics of ENSO Extremes and the Strong 2015/2016 El Niño, *Rev. Geophys.*, 55, 1079–1129, <https://doi.org/10.1002/2017rg000560>, 2017.
- Schoeberl, M. R., Douglass, A. R., Newman, P. A., Lait, L. R., Lary, D., Waters, J., Livesey, N., Froidevaux, L., Lambert, A., Read, W., Filipiak, M. J., and Pumphrey, H. C.: QBO and annual cycle variations in tropical lower stratosphere trace gases from HALOE and Aura MLS observations, *J. Geophys. Res.: Atmos.*, 113, <https://doi.org/10.1029/2007jd008678>, 2008.
- Siddiqui, T. A., Chau, J. L., Stolle, C., and Yamazaki, Y.: Migrating solar diurnal tidal variability during Northern and Southern Hemisphere Sudden Stratospheric Warmings, *Earth Planets Space*, 74, <https://doi.org/10.1186/s40623-022-01661-y>, 2022.
- Singh, D. and Gurubaran, S.: Variability of diurnal tide in the MLT region over Tirunelveli (8.7° N), India: Consistency between ground- and space-based observations, *J. Geophys. Res.: Atmos.*, 122, 2696–2713, <https://doi.org/10.1002/2016jd025910>, 2017.
- Smith, A. K.: Global Dynamics of the MLT, *Surv. Geophys.*, 33, 1177–1230, <https://doi.org/10.1007/s10712-012-9196-9>, 2012.
- Smith, A. K., Harvey, V. L., Mlynarczyk, M. G., Funke, B., García-Comas, M., Hervig, M., Kaufmann, M., Kyrölä, E., López-Puertas, M., McDade, I., Randall, C. E., Russell, J. M., Sheese, P. E., Shiotani, M., Skinner, W. R., Suzuki, M., and Walker, K. A.: Satellite observations of ozone in the upper mesosphere, *J. Geophys. Res.: Atmos.*, 118, 5803–5821, <https://doi.org/10.1002/jgrd.50445>, 2013.
- Smith, A. K., Pedatella, N. M., Marsh, D. R., and Matsuo, T.: On the Dynamical Control of the Mesosphere–Lower Thermosphere by the Lower and Middle Atmosphere, *J. Atmos. Sci.*, 74, 933–947, <https://doi.org/10.1175/jas-d-16-0226.1>, 2017.
- Somerville, R. C. J., Stone, P. H., Halem, M., Hansen, J. E., Hogan, J. S., Druyan, L. M., Russell, G., Lacis, A. A., Quirk, W. J., and Tenenbaum, J.: The GISS Model of the Global Atmosphere, *J. Atmos. Sci.*, 31, 84–117, [https://doi.org/10.1175/1520-0469\(1974\)031<0084:Tgmotg>2.0.Co;2](https://doi.org/10.1175/1520-0469(1974)031<0084:Tgmotg>2.0.Co;2), 1974.
- Sun, R., Gu, S., Dou, X., and Li, N.: Tidal Structures in the Mesosphere and Lower Thermosphere and Their Solar Cycle Variations, *Atmosphere*, 13, <https://doi.org/10.3390/atmos13122036>, 2022.
- Stober, G., Kuchar, A., Pokhotelov, D., Liu, H., Liu, H.-L., Schmidt, H., Jacobi, C., Baumgarten, K., Brown, P., Janches, D., Murphy, D., Kozlovsky, A., Lester, M., Belova, E., Kero, J., and Mitchell, N.: Interhemispheric differences of mesosphere–lower thermosphere winds and tides investigated from three whole-atmosphere models and meteor radar observations, *Atmos. Chem. Phys.*, 21, 13855–13902, <https://doi.org/10.5194/acp-21-13855-2021>, 2021.
- Strobel, D. F.: Parameterization of the atmospheric heating rate from 15 to 120 km due to O<sub>2</sub> and O<sub>3</sub> absorption of solar radiation, *J. Geophys. Res.: Oceans*, 83, 6225–6230, <https://doi.org/10.1029/JC083iC12p06225>, 1978.
- Tweedy, O. V., Kramarova, N. A., Strahan, S. E., Newman, P. A., Coy, L., Randel, W. J., Park, M., Waugh, D. W., and Frith, S. M.: Response of trace gases to the disrupted 2015–2016 quasi-biennial oscillation, *Atmos. Chem. Phys.*, 17, 6813–6823, <https://doi.org/10.5194/acp-17-6813-2017>, 2017.
- Vincent, R. A., Kovalam, S., Fritts, D. C., and Isler, J. R.: Long-term MF radar observations of solar tides in the low-latitude mesosphere: Interannual variability and comparisons with the GSWM, *J. Geophys. Res.: Atmos.*, 103, 8667–8683, <https://doi.org/10.1029/98jd00482>, 1998.
- Wang, J., Li, N., Yi, W., Xue, X., Reid, I. M., Wu, J., Ye, H., Li, J., Ding, Z., Chen, J., Li, G., Tian, Y., Chang, B., Wu, J., and Zhao, L.: The impact of quasi-biennial oscillation (QBO) disruptions on diurnal tides over the low- and mid-latitude mesosphere and lower thermosphere (MLT) region observed by a meteor radar chain, *Atmos. Chem. Phys.*, 24, 13299–13315, <https://doi.org/10.5194/acp-24-13299-2024>, 2024.

- Wang, Y., Rao, J., Lu, Y., Ju, Z., Yang, J., and Luo, J.: A revisit and comparison of the quasi-biennial oscillation (QBO) disruption events in 2015/16 and 2019/20, *Atmos. Res.*, 294, <https://doi.org/10.1016/j.atmosres.2023.106970>, 2023.
- Wu, D. L., McLandress, C., Read, W. G., Waters, J. W., and Froidevaux, L.: Equatorial diurnal variations observed in UARS Microwave Limb Sounder temperature during 1991–1994 and simulated by the Canadian Middle Atmosphere Model, *J. Geophys. Res.: Atmos.*, 103, 8909–8917, <https://doi.org/10.1029/98jd00530>, 1998.
- Wu, Q., Ortland, D. A., Killeen, T. L., Roble, R. G., Hagan, M. E., Liu, H. L., Solomon, S. C., Xu, J., Skinner, W. R., and Niciejewski, R. J.: Global distribution and interannual variations of mesospheric and lower thermospheric neutral wind diurnal tide: 1. Migrating tide, *J. Geophys. Res.: Space Phys.*, 113, <https://doi.org/10.1029/2007ja012542>, 2008.
- Xu, J., Smith, A. K., Yuan, W., Liu, H. L., Wu, Q., Mlynczak, M. G., and Russell, J. M.: Global structure and long-term variations of zonal mean temperature observed by TIMED/SABER, *J. Geophys. Res.*, 112, <https://doi.org/10.1029/2007jd008546>, 2007.
- Xu, J., Smith, A. K., Liu, H. L., Yuan, W., Wu, Q., Jiang, G., Mlynczak, M. G., Russell, J. M., and Franke, S. J.: Seasonal and quasi-biennial variations in the migrating diurnal tide observed by Thermosphere, Ionosphere, Mesosphere, Energetics and Dynamics (TIMED), *J. Geophys. Res.*, 114, <https://doi.org/10.1029/2008jd011298>, 2009.
- Xu, J., Smith, A. K., Jiang, G., and Yuan, W.: Seasonal variation of the Hough modes of the diurnal component of ozone heating evaluated from Aura Microwave Limb Sounder observations, *J. Geophys. Res.: Atmos.*, 115, <https://doi.org/10.1029/2009jd013179>, 2010.
- Yang, C., Smith, A. K., Li, T., and Dou, X.: The Effect of the Madden – Julian Oscillation on the Mesospheric Migrating Diurnal Tide: A Study Using SD – WACCM, *Geophys. Res. Lett.*, 45, 5105–5114, <https://doi.org/10.1029/2018gl077956>, 2018.
- Zhu, X.: An Accurate and Efficient Radiation Algorithm for Middle Atmosphere Models, *J. Atmos. Sci.*, 51, 3593–3614, [https://doi.org/10.1175/1520-0469\(1994\)051<3593:Aaaera>2.0.Co;2](https://doi.org/10.1175/1520-0469(1994)051<3593:Aaaera>2.0.Co;2), 1994.